A systematic local view of the long-term changes of the atmospheric energy cycle

A Systematic Local View of the Long-Term Changes in the Atmospheric Energy Cycle

ZHEN LIU,[a,b,c] CHRISTIAN L. E. FRANZKE,[b,c] LENKA NOVAK,[d] REMI TAILLEUX,[e] AND VALERIO LEMBO[f]

[a] *Earth, Ocean and Atmospheric Sciences Thrust, Function Hub, Hong Kong University of Science and Technology (Guangzhou), Guangzhou, China*
[b] *Center for Climate Physics, Institute for Basic Science, Busan, South Korea*
[c] *Pusan National University, Busan, South Korea*
[d] *California Institute of Technology, Pasadena, California*
[e] *Department of Meteorology, University of Reading, Reading, United Kingdom*
[f] *Consiglio Nazionale delle Ricerche, Istituto di Scienze dell'Atmosfera e del Clima, Bologna, Italy*

(Manuscript received 22 February 2024, in final form 24 July 2024, accepted 28 August 2024)

ABSTRACT: The global climatology and long-term changes in the atmospheric energy cycle in the boreal winter are analyzed using a local available potential energy framework using the fifth-generation ECMWF reanalysis data during 1979–2021. In contrast to the classic Lorenz energy cycle, this local framework provides the local information of available potential energy (APE) and its interactions with kinetic energy (KE), allowing the systematic study of barotropic and baroclinic processes. A further systematic decomposition of the APE and KE reservoirs into high- and low-frequency components is conducted to investigate the source and sink terms that account for their spatial variations and long-term changes. The climatology of the local energetic budget terms shows that the interplay between low-frequency APE and KE is mostly over the tropical and polar regions associated with the thermally direct circulation there. Interactions involving high-frequency components are mainly located in the storm-track regions. We show that under recent global warming, a prominent dipolar trend of changes is present over the Asia–Pacific region for all energy forms. The long-term changes in the energy budget reveal how high-frequency APE intensification is due to a stronger conversion from low-frequency APE upstream of the storm track and that this intensification can be compensated by eddy advection away from the storm track, rather than conversion to kinetic energy in the proximity of the mean jet. This provides evidence that a warmer climate substantially affects the energy cycle and, thus, the atmospheric circulation.

SIGNIFICANCE STATEMENT: Potential and kinetic energies are major components of atmospheric circulation. Those energies and their generation, dissipation, and conversions provide insight into the dynamics of atmospheric circulation. The Lorenz energy cycle, based on a global framework, has been fundamental in deepening our understanding of the atmosphere. However, here we use a systematic local framework to gain a better understanding of atmospheric circulation changes and how global warming has affected them. Our study finds a general intensification of the local energy cycle over the last few decades.

KEYWORDS: Atmospheric circulation; Dynamics; Energy transport; Climate variability; Trends

1. Introduction

The intricate interplay between solar insolation, atmospheric circulation patterns, and the redistribution of energy shapes our daily weather, regional climate, and ecosystems. Understanding of the fundamental processes that govern the transformation and redistribution of energy within the atmosphere is crucial for unraveling the complex dynamics of weather and climate systems and their response to external forcings. A seminal work that has remarkably contributed to this field is the introduction of the globally defined theory of available potential energy (APE) (Lorenz 1955b). Physically, the APE represents the maximum of potential energy available for reversible conversions into kinetic energy (KE) (Tailleux 2013). This approach, exemplified by the widely accepted four-box Lorenz energy cycle (LEC), provides valuable insights into the relationships between eddy KE and eddy APE with respect to zonal-mean KE and APE. In most models, the LEC is dominated by the energy conversion pathways pertaining to baroclinic unstable eddies associated with storm-track dynamics (Oort and Peixoto 1976; Li et al. 2007). Presumably, the LEC is likely modulated by exchanges unrelated to storm-track dynamics, but their relative importance is difficult to quantify in a globally defined APE framework. To understand these, a local view of APE, not restricted to any specific type of "mean" and capable of describing the local energy transformations across various spatial and temporal scales, is a priori needed, but has remained uncommon. As the mean atmospheric circulation is far from zonal, how to interpret the LEC and its responses to climate change is far from straightforward in the global APE framework. In this paper, we show that investigating the issue from a

Denotes content that is immediately available upon publication as open access.

Supplemental information related to this paper is available at the Journals Online website: https://doi.org/10.1175/JCLI-D-24-0106.s1.

Corresponding author: Christian L. E. Franzke, christian.franzke@pusan.ac.kr

DOI: 10.1175/JCLI-D-24-0106.1

local APE viewpoint is useful to get detailed insights into the nature of the LEC. The LEC and globally defined APE theory have played a pivotal role in assessing the global energy budget using reanalysis datasets (Li et al. 2007; Marques et al. 2010; Kim and Kim 2013; Pan et al. 2017; Ma et al. 2021), historical model simulations (Boer and Lambert 2008; Lembo et al. 2019), and climate model projections (Ahbe and Caldeira 2017; Michaelides 2021; Kanno and Iwasaki 2022). However, the global character of APE and its focus on the zonal-mean circulation are increasingly recognized as important limitations of the framework, owing to the difficulties in linking the volume-integrated energy pathways to regional ones. Attempts to adopt a regional perspective on APE estimation have been made (e.g., Oort and Peixoto 1976; Li et al. 2007; Ahbe and Caldeira 2017), but few studies have used a rigorously derived local APE framework.

These conceptual difficulties and limitations associated with the global APE framework prompted the quest for local available energetics. The possibility to construct Lorenz APE theory from a local principle was first established by Holliday and McIntyre (1981), Andrews (1981), and Shepherd (1993); see also Tailleux (2013, 2018) for a review and most recent formulation. In contrast to the global APE theory, the local APE theory defines the total APE of a system as the volume integral of a positive definite APE density. Physically, the APE density of a fluid parcel represents the path-independent work against buoyancy forces (defined relative to a Lorenz reference state density field) needed to move a fluid parcel from its reference position to its actual position. Because the APE density represents a fundamental property of a fluid parcel, it is physically meaningful to speak of its advection, diffusion, conversion with kinetic energy, or fluxes through regional boundaries, which is not possible with the sign indefinite integrand of the global APE theory.

Importantly, the local APE framework is not restricted to any specific type of mean. By defining the concept of an "eddy" relative to a temporal mean, ensemble means, or other types of mean, the local theory provides a versatile and adaptable framework for systematically investigating regional energy conversions not necessarily restricted to storm-track dynamics in many new and different ways. The usefulness of the approach was first demonstrated by Kucharski and Thorpe (2000) and then by Novak and Tailleux (2018), which provided a three-dimensional representation of local APE density and its budget terms using the ERA-Interim reanalysis dataset. The globally integrated local APE can be easily computed using pressure-level datasets with higher accuracy than the traditional calculation of Lorenz APE on isobaric surfaces under the quasigeostrophic approximation. One key insight revealed by the local APE framework that had remained inaccessible to the global APE framework is the importance of the advection of APE in the storm-track regions (Novak and Tailleux 2018) or in the core region of tropical cyclones (Harris et al. 2022).

In this study, we aim to present a comprehensive analysis of the local APE framework, focusing on its interactions with kinetic energy terms, which inherently possess a local nature. In fact, the multiscale nature of atmospheric eddies (e.g., Faranda et al. 2018; Lovejoy 2019; Franzke et al. 2020) implies that all scales reproduce the same features of energy conversions within eddies and that energy is transferred upscale and downscale along a known kinetic energy cascade.

We utilize the fifth major global reanalysis produced by ECMWF (ERA5; Hersbach et al. 2020) to examine the climatology and long-term changes in energetic terms, offering a holistic depiction of the atmospheric energy cycle within this local energetic framework. Building upon the work of Novak and Tailleux (2018), our study not only presents a complete cycle of the local energetic framework but also investigates its observed changes over the last few decades. By providing a benchmark for understanding large-scale circulation changes through the local APE framework, this work will contribute to the advancement of atmospheric energetic research. The remainder of this paper is organized as follows: Section 2 provides a brief introduction to the data and methodology employed; section 3 documents the climatology of energetic terms and their budget components; section 4 discusses the observed long-term changes in local energetics; and finally, section 5 concludes with a summary and further discussion.

2. Data and methods

a. Data

To analyze the energy cycle, we use the daily ERA5 dataset covering the period 1979–2021 at a horizontal resolution of 1°, with 20 vertical pressure levels up to 50 hPa (Hersbach et al. 2020). We also tried more vertical levels extending up to 10 hPa. However, the results are similar, suggesting that the 20 levels we considered are enough to get robust results. The principal atmospheric fields used include horizontal and vertical wind, temperature, and geopotential. Energetic terms are first computed using daily data and then aggregated into seasonal means. We focus on the boreal winter (December–February), when the jet stream and eddies are stronger in the Northern Hemisphere.

b. Definition of low-frequency and high-frequency APE and KE densities

As documented in Novak and Tailleux (2018), the original atmospheric fields (e.g., temperature) are decomposed into low-frequency and high-frequency components using a 10-day low-pass Lanczos filter. Then, the low- and high-frequency APE densities can be calculated separately based on filtered fields. As APE is not a quadratic quantity, unlike KE, a nonconventional low-frequency reference state of pressure $\tilde{p}_r$ is required for the separation into low-frequency and high-frequency components. The term $\tilde{p}_r$ should satisfy $\overline{\theta}_r(\tilde{p}_r, t) = \overline{\theta}$ and mirror the dimensions of $\overline{\theta}$, with the overbar and tilde denoting the 10-day low-pass filter and nonconventional low-frequency mean, respectively. Hence, the expressions of low-frequency and high-frequency APEs can be written as

$$P_L = \int_{\tilde{p}_r}^{p} \{\alpha(\overline{\theta}, p) - \alpha[\overline{\theta}_r(p, t), p]\} dp, \tag{1}$$

$$P_H = \overline{\int_{p_r}^{\tilde{p}_r} \{\alpha(\theta, p) - \alpha[\theta_r(p, t), p]\} dp}. \quad (2)$$

Here, α is the specific volume, θ is potential temperature, p_r is the reference state pressure using the isobaric averaging method, and the subscript r denotes the reference state.

We also apply the low-pass filter on zonal u and meridional v components of the wind to get their low-frequency and high-frequency parts. The high-frequency component, denoted by the prime in Eq. (4), is estimated as the residual between the original field and its low-frequency part. Thus, the expressions of low-frequency and high-frequency KEs are

$$K_L = \frac{1}{2}(\overline{u}^2 + \overline{v}^2), \quad (3)$$

$$K_H = \frac{1}{2}(\overline{u'^2} + \overline{v'^2}). \quad (4)$$

Note that this study exclusively focuses on the low-frequency component of high-frequency KE in order to establish stronger links with high-frequency APE and consequently complete the energy cycle. The global-mean high-frequency component of KE constitutes merely one and a half parts per 10 000 of the low-frequency components. Furthermore, we examined the cross-scale interaction term $\overline{u}u' + \overline{v}v'$, which is only at a magnitude of approximately 3% of total KE and thus is neglected in the energy cycle.

c. Detailed expressions of the local energetic framework

In this part, the budget equations for various forms of energy are expressed mainly according to Novak and Tailleux (2018) and Novak (2016), where the detailed derivation can be found. However, we made some reformulations in the calculations of some terms of the APE budget including the eddy advection term in the high-frequency APE budget and diabatic heating term. The eddy advection term in Eq. (29) in Novak and Tailleux (2018) is calculated as a divergence term $-\nabla \cdot (\overline{\mathbf{V}'P_T'})$ assuming the high-frequency component of wind is nondivergent. Furthermore, the diabatic term is explicitly estimated as the total derivative of potential temperature in our calculations but is treated as a residual in Novak and Tailleux (2018). We found that the budget is better closed after making this adjustment; hence, our residuals are smaller.

The budget of low-frequency and high-frequency APEs is written in the form as described in Novak and Tailleux (2018):

$$\frac{\partial P_L}{\partial t} = \underbrace{-\overline{\mathbf{V}} \cdot \nabla P_L}_{\text{Advection}} + \underbrace{\overline{\delta\alpha}\,\overline{\omega}}_{C(K_L, P_L)} \underbrace{-C_p \tilde{\gamma} \frac{\overline{T}}{\overline{\theta}} \nabla \cdot \overline{\mathbf{V}'\theta'}}_{C(P_H, P_L)} \underbrace{-\tilde{\chi} + \tilde{\gamma}\overline{Q}}_{\text{Diabatic}}, \quad (5)$$

$$\frac{\partial P_H}{\partial t} = \underbrace{-\overline{\mathbf{V}} \cdot \nabla P_H}_{\text{Mean advection}} \underbrace{-\overline{\mathbf{V}' \cdot \nabla P_T'}}_{\text{Eddy advection}} + \underbrace{\overline{\delta\alpha'\omega'}}_{C(K_H, P_H)} + \underbrace{C_p \tilde{\gamma} \frac{\overline{T}}{\overline{\theta}} \nabla \cdot \overline{\mathbf{V}'\theta'}}_{C(P_L, P_H)} + \underbrace{\overline{\gamma}\overline{Q} + \overline{\gamma' Q'} - \tilde{\gamma}\overline{Q} + \tilde{\chi} - \overline{\chi}}_{\text{Diabatic}}. \quad (6)$$

Here, t is the time; $\mathbf{V} = (u, v, \omega)$ is the three-dimensional wind in both horizontal and vertical coordinates; $P_T = P_L + P_H$ is the total APE; δ represents the differences with respect to the reference state; ω is the vertical pressure velocity; C_p is the specific heat capacity at constant pressure; γ is the thermal efficiency in Eq. (7), which is the same as that in Lorenz (1955a); χ is the additional diabatic term associated with temporal changes in the reference state in Eq. (8); and Q is the diabatic heating rate. The terms γ and χ are calculated as follows:

$$\gamma = \frac{T - T_r}{T}, \quad (7)$$

$$\chi = \int_{p_r}^{p} \frac{\partial_r}{\partial t} dp. \quad (8)$$

The physical meanings of the terms of Eq. (5) from left to right are as follows: local temporal tendency of low-frequency APE indicating how low-frequency APE will change, mean advection of low-frequency APE which horizontally transports APE, conversions from low-frequency KE to APE, conversions from high-frequency to low-frequency APEs, and diabatic heating terms which generate low-frequency APE. The interpretations of the terms of Eq. (6) are as follows: local temporal tendency of high-frequency APE indicating how high-frequency APE will change, mean advection of high-frequency APE and eddy advection of total APE which both describe the horizontal transport of APE, conversions from high-frequency KE to APE, conversions from low-frequency to high-frequency APEs, and diabatic heat terms which describe the generation of high-frequency APE.

The budget of low-frequency and high-frequency KEs follows that given in Novak (2016):

$$\frac{\partial K_L}{\partial t} = \underbrace{-\overline{\mathbf{V}} \cdot \nabla K_L}_{\text{Advection}} + \underbrace{\overline{\mathbf{V}_h'\mathbf{V}_h'} \cdot \nabla \overline{\mathbf{V}}_h}_{C(K_H, K_L)} \underbrace{-\nabla \cdot (\overline{\mathbf{V}}_h \overline{\mathbf{V}_h'\mathbf{V}_h'})}_{\text{Divergence}} \underbrace{-\overline{\mathbf{V}} \cdot \nabla \overline{\delta\Phi}}_{\text{Geopotential advection}} \underbrace{-\overline{\delta\alpha}\,\overline{\omega}}_{C(P_L, K_L)} + \underbrace{\overline{\mathbf{V}}_h \overline{\mathbf{F}}}_{\text{Friction flux}}$$

$$\underbrace{-\frac{\overline{v}\overline{u'u'} - \overline{u}\,\overline{u'v'}}{a}\tan\phi + \frac{\overline{u}(\overline{u}\,\overline{\omega} + \overline{u'\omega'}) + \overline{v}(\overline{v}\,\overline{\omega} + \overline{v'\omega'})}{a\rho g}}_{\text{Spherical}}, \quad (9)$$

$$\frac{\partial K_H}{\partial t} = \underbrace{-\overline{\mathbf{V}}\cdot\nabla K_H}_{\text{Mean advection}} \underbrace{-\overline{\mathbf{V}'\cdot\nabla K_H}}_{\text{Eddy advection}} \underbrace{-\overline{\mathbf{V}'_h\mathbf{V}'_h}\cdot\nabla\overline{\mathbf{V}}_h}_{C(K_L,\,K_H)} \underbrace{-\overline{\mathbf{V}'\cdot\nabla\delta\Phi'}}_{\text{Geopotential advection}} \underbrace{-\overline{\delta\alpha'\omega'}}_{C(P_H,\,K_H)} + \underbrace{\overline{\mathbf{V}'_h\mathbf{F}'}}_{\text{Friction flux}}$$

$$\underbrace{-\frac{\overline{u}\,\overline{u'v'}-\overline{v}\,\overline{u'u'}}{a}\tan\phi+\frac{\overline{\omega}\,\overline{u'u'}+\overline{u}\,\overline{u'\omega'}+\overline{v}\,\overline{v'\omega'}+\overline{\omega}\,\overline{v'v'}}{a\rho g}}_{\text{Spherical}}. \tag{10}$$

Note that our discussion of energetics assumes atmospheric motions to satisfy the hydrostatic primitive equations. As is well known, closing the energy budget of these equations requires neglecting the vertical component of velocity. The Coriolis force is normal to the horizontal velocity field and therefore does not contribute to the kinetic energy budget (Persson 2005; Broström et al. 2014). Here, $\mathbf{V}_h = (u, v)$ is the horizontal wind; ϕ is the latitude; Φ is the geopotential; g is the gravitational constant; ρ is the air density; and $\mathbf{F} = (F_x, F_y)$ represents frictional forces.

The physical meanings of the terms of Eq. (9) from left to right are as follows: local temporal tendency of low-frequency KE, mean advection of low-frequency KE, conversions from high-frequency to low-frequency KEs, horizontal divergence of the high-frequency momentum flux, mean advection of low-frequency geopotential anomaly with respect to the reference state, conversions from low-frequency APE to KE, the friction flux, and terms associated with the spherical geometry. The interpretations of the terms of Eq. (10) are as follows: local temporal tendency of high-frequency KE, mean advection of high-frequency KE, eddy advection of high-frequency KE, conversions from low-frequency to high-frequency KEs, low-frequency eddy advection of high-frequency geopotential anomaly with respect to the reference state, conversions from high-frequency APE to KE, the friction flux, and terms associated with spherical geometry.

d. Long-term changes

The statistical significance levels of long-term changes in the energetic terms and their budget between two different time epochs (i.e., 2007–21 and 1980–94) are estimated by the two-sided Student's t test. A 10-day Lanczos (Duchon 1979) filter is implemented to the original atmospheric fields to eventually partition the APE and KE terms into low and high frequencies, thereby enabling us to investigate interactions between synoptic-scale (i.e., high-frequency) waves and Rossby (i.e., low-frequency) waves associated with synoptic-scale weather systems and the slowly varying circulation, respectively.

3. Climatology of the atmospheric energetics

a. Climatology of APE and KE terms

Figure 1 shows the spatial distribution of the boreal winter climatology of APE and KE and their interannual standard deviations. The APE and KE terms are further partitioned into low-frequency (periods of more than 10 days) and high-frequency (periods of less than 10 days) parts, which are denoted by subscripts L and H, respectively. Along with their budget terms, the energetic interactions between the transient disturbances on synoptic scales and low-frequency Rossby waves (i.e., L = low-frequency waves + zonal mean flow) can be explicitly evaluated. The centers of P_L are mostly concentrated over the high-latitude region north of 60°N with maximum amplitude in the upper troposphere at 400 hPa (Figs. 1a,e). Interestingly, this vertical distribution contrasts with that of the classical Lorenz energy cycle, which shows a maximum of the zonal-mean APE near the surface in polar regions (Peixóto and Oort 1974; Li et al. 2007; Kim and Kim 2013). It is mainly because the local APE is defined as the integrated buoyancy force for each air parcel between the actual level and the reference level of pressure. The reference pressure level should satisfy $\overline{\theta}_r(\tilde{p}_r, t) = \overline{\theta}$. The reference state pressure of each air parcel depends on the differences between the actual state and the reference state (i.e., isobaric mean) of the low-frequency potential temperature (Figs. S1a,b in the online supplemental material). The negative potential temperature anomalies indicate that the air parcel needs to descend to reach the reference state and vice versa over the tropics. Despite the larger negative anomalies near the surface over the Arctic, the air parcel there can only descend toward the lowest pressure level (i.e., 1000 hPa at maximum). That is why the differences between p and $\tilde{p}_r$ are relatively small near the surface (Fig. S1d). By contrast, they are much larger in the upper troposphere around 300 hPa over the Arctic. Positive and negative values of differences in pressure between the actual and low-frequency reference states indicate how far the parcel would need to travel to reach its level of neutral buoyancy on these low-frequency time scales. As the differences are marginal near the surface (Fig. S1d), P_L has a relatively small magnitude according to Eq. (1). Overall, P_L is more sensitive to the pressure difference between the actual and reference states than potential temperature differences. We also note that most previous studies on the classical LEC providing a local view of APE assume that the globally defined LEC can also be interpreted in a local sense, even though this contradicts the derivation of the LEC (Novak and Tailleux 2018). Horizontally, the P_L peaks are mainly located at the regions (e.g., northeastern Russia and Greenland) with relatively lower temperature (Kållberg et al. 2005). This is expected as APE is intimately related to a horizontally invariant reference state based on isobaric mean potential temperature. This is also the reason for the second maximum over the tropics and the minimum of APE in midlatitudes between 30° and 60°

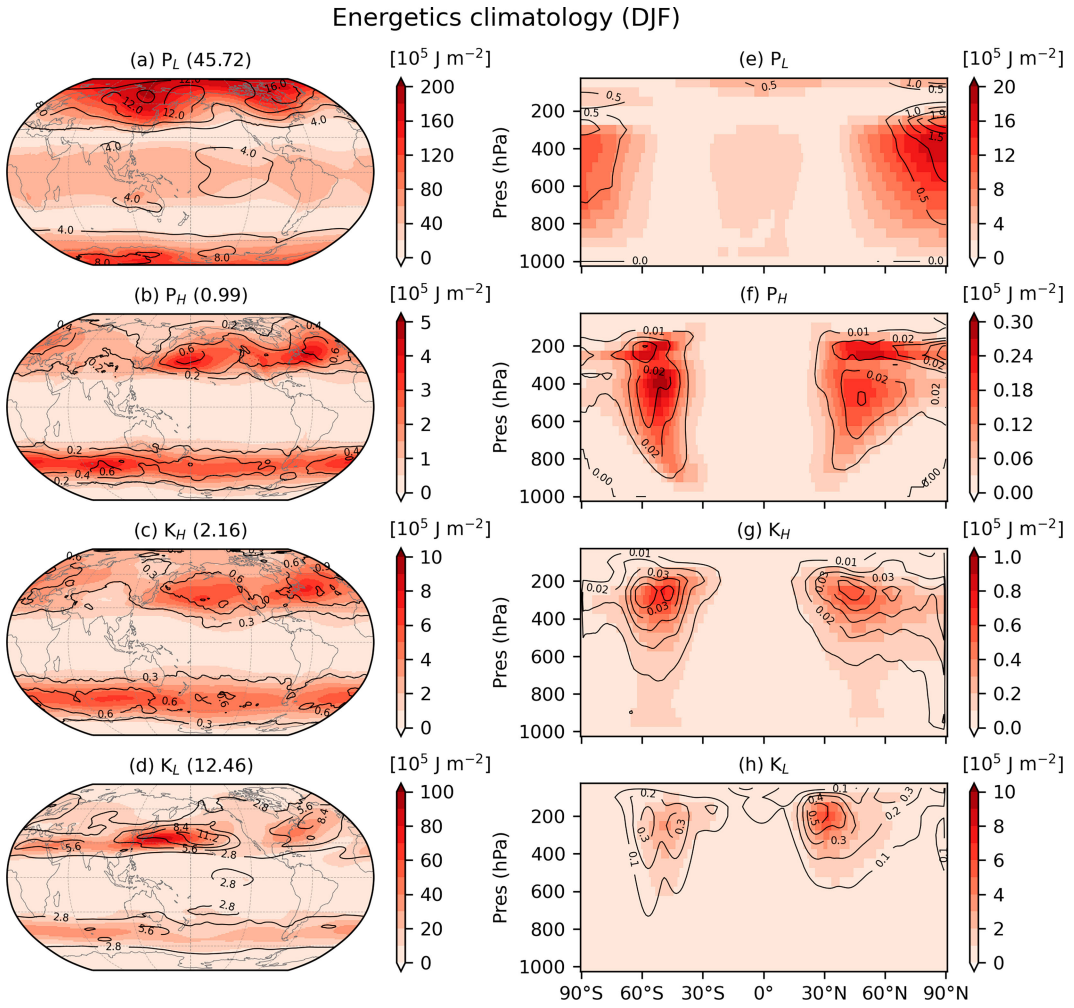

FIG. 1. The spatial distribution of the vertically integrated (1000–50 hPa; mass-weighted) climatological (a) low-frequency APE P_L (shading), (b) high-frequency APE P_H, (c) high-frequency APE K_H, and (d) low-frequency KE K_L in the boreal winter (December–February) during 1980–2021. (e)–(h) As in (a)–(d), but for zonal average over the globe. The values in parentheses represent the global mean of energetic terms. The contours denote the annual standard deviation, and the units of these energetic terms are in 10^5 J m^{-2}.

depending on the potential temperature departure from the isobaric mean. Overall, the pattern of P_L follows that of the pressure differences between the actual state and the low-frequency reference state (Fig. S1c). The centers of the interannual standard deviation in high latitudes are well collocated with the large P_L areas horizontally but vertically shifted slightly upward (Figs. 1a,e). The maxima in high-frequency APE P_H are located in the midlatitudes, close to the storm tracks. They are concentrated over the downstream region of the P_L centers to the south, such as the northwestern Pacific, the northwestern Atlantic, and the northern part of the Southern Ocean (Fig. 1b), suggesting important conversions from low-frequency to high-frequency APEs. In the global average, P_H is one forty-fifth of P_L. The adjacent locations of high-frequency APE maxima and storm tracks (i.e., high-frequency KE in Fig. 1c) indicate a close association between them. The corresponding energy conversion terms will be discussed in more detail in the next section. Vertically, there are two peaks at 500 and 200 hPa in the middle of the troposphere and the lower stratosphere, respectively (Fig. 1f). The peaks of the P_H standard deviations generally follow their maximum values. These findings are consistent with those in Novak and Tailleux (2018) based on the ERA-Interim reanalysis dataset.

In the distribution of K_H, there are two maxima over the North Pacific and North Atlantic regions in the Northern Hemisphere matching up with locations of the storm tracks at around 300 hPa (Figs. 1c,g), where strong transient disturbances occur. Note that the Pacific K_H center is less collocated with the P_H maximum than that over the Atlantic (Fig. 1c). There are two centers of standard deviation residing on the northward and southward sides of the K_H peaks (Fig. 1g), indicating a meridional oscillation of storm tracks on the interannual time scale. Upstream and equatorward of the K_H maxima, K_L peaks over the northwestern Pacific and the

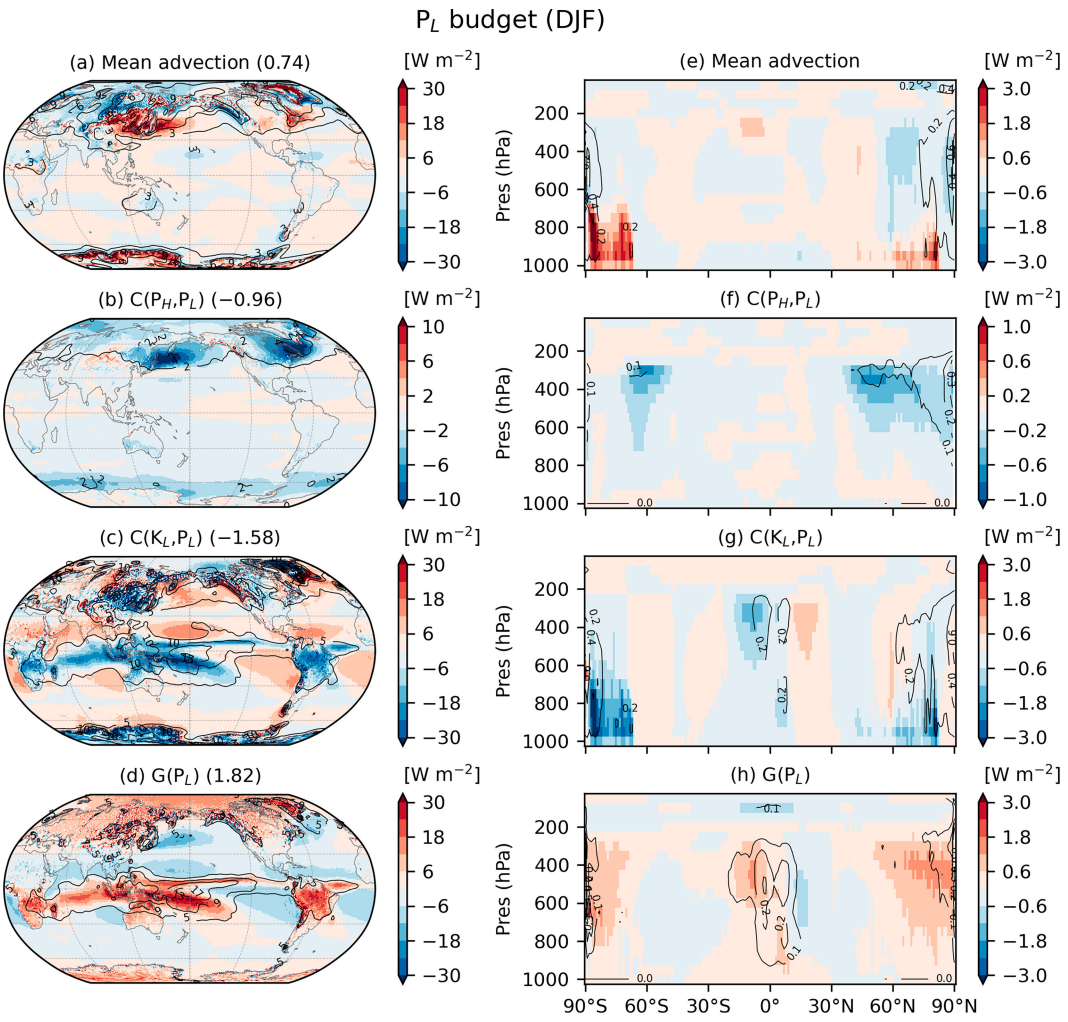

FIG. 2. The distribution of climatological budget terms for low-frequency APE (W m^{-2}). Vertically integrated (1000–50 hPa; mass-weighted) (a) mean advection (shading), (b) conversion from high-frequency to low-frequency APEs $C(P_H, P_L)$, (c) conversion from low-frequency KE to APE $C(K_L, P_L)$, and (d) generation of low-frequency APE $G(P_L)$ in the boreal winter (December–February) during 1980–2021. (e)–(h) As in (a)–(d), but for zonal averages over the globe. The values in parentheses represent the global mean of conversion terms. The contours denote the annual standard deviation.

northwestern Atlantic, showing the location of the jet stream (Figs. 1d,h). Differently from the Pacific jet, a clear separation between the subtropical and eddy-driven jets is seen over the Atlantic (Fig. 1d), identifying the split jet structure. The standard deviations are shifted northward and to the downstream area of the K_L maxima, overlapping with the storm-track centers. Momentum converges there and feeds back onto the low-frequency circulation which sustains the jet. In the latitude–pressure cross-sectional plot, two standard deviation centers are displayed on the northern and southern sides of the K_L peaks over the Southern Hemisphere but not over the Northern Hemisphere (Fig. 1h) where the jet may vary more in terms of intensity on interannual time scales during the boreal winter. This splitting feature of the jet over the Southern Hemisphere is also visible in K_H (Fig. 1g). Note that K_L is dominated by the subtropical jet that could be due to the fact that K_L captures the dynamics of the waveguide of the subtropical jet. The magnitude of KE in transient disturbances is about one-sixth of that of the low-frequency circulation on global average.

b. *Climatology of low-frequency APE budget terms*

Figure 2 shows the distribution of the budget terms for P_L according to Eq. (5). Note that we show terms with a relatively small magnitude in supplementary figures (i.e., local tendency in Fig. S2). The negligible role of the residual term, estimated as the differences between the local tendency term and the sum of the terms on the right-hand side of Eq. (5), shows that the P_L budget is well closed, and moreover, the residue is mostly situated in the stratosphere.

Large anomalies of the mean advection mainly appear in the midlatitudes, where there is concurrent occurrence of

strong winds and a large P_L gradient in the Northern Hemisphere (Fig. 2a). There are two salient positive anomalies of mean advection terms: One is over eastern China extending eastward toward the Pacific across Japan; and the other is over the eastern United States and the northwestern Atlantic. We further decompose the mean advection into different components in meridional, zonal, and vertical directions (Fig. S3). Interestingly, a generally strong compensation is revealed between the meridional and zonal components, with relatively small contributions coming from the vertical component. The positive anomalies over land are mainly related to meridional advection on the western side of the P_L peaks associated with northerly cold air intrusion, while those over the downstream ocean are mostly associated with zonal advection on the P_L peaks by the westerlies, consistent with cold air outbreaks. Near the poles, positive anomalies in the lower atmosphere are mostly attributed to the vertical component due to the extremely cold continents, such as Greenland and Antarctica (Figs. 2a,e). The visible downward motion there would transport P_L from the mid- to lower tropospheres along the gradient. Theoretically, the advection term should integrate to zero globally under the assumption of mass conservation, in which case the volume-integrated budget equations would reduce to those of the classical LEC budget. This assumption is the backbone of the classic LEC budget, which uses globally integrated terms. The terms associated with spherical geometry in the kinetic energy budget are either canceled out or often neglected because of their small magnitude (Oort 1964). Then, the sum of APE and KE will be conserved under frictionless and adiabatic flow. The nonzero advection part mainly comes from the vertical component (Figs. S3e,h) and resembles positive anomalies of wind convergence, mostly the low-frequency component (Figs. S4c,d). Note that the vertical velocity may not be reliable over Greenland and Antarctica due to some data artifacts and our method of using coarse vertical integrals in stable boundary layers over complex terrain. The nonzero values of convergence mean that the continuity equation is not satisfied, and thus, the mass and energy are not totally conserved. This is a common problem in the reanalysis due to data assimilation (Hersbach et al. 2020). Although methods have been proposed to correct mass and energy conservation issues in reanalysis products (Trenberth et al. 2009), implementing these in practice represents a major undertaking that we did not attempt in this study. For this reason, the globally integrated values estimated using reanalysis may not be reliable and should therefore be interpreted with caution. Although such a limitation has remained largely unnoticed so far, it should be noted that all published studies of the classic LEC based on uncorrected reanalysis products may be affected. A key hypothesis of this study is that local energy conversions are only affected at the second order by mass and energy conservation errors in reanalysis products and therefore more reliable. The standard deviations mainly peak in the polar regions in the mid–upper troposphere, which likely depends on the P_L values (Fig. 2a).

The pattern of interactions between P_H and P_L [i.e., $-C_p\tilde{\gamma}(\overline{T}/\overline{\theta})\nabla\cdot\overline{\mathbf{V}'\theta'}$] remarkably resembles that of P_H but is slightly shifted to the north, such as strong anomalies over the northwestern Pacific, the northwestern Atlantic, and the northern Southern Ocean (Figs. 2b,f, and 1b,f). Negative anomalies denote conversions from P_L to P_H, indicating that P_L is the main source of P_H. The principal terms accounting for $C(P_L, P_H)$ are thermal efficiency $\tilde{\gamma}$ and divergence of heat transport by transient eddies $\nabla\cdot\overline{\mathbf{V}'\theta'}$ from its expression in Eq. (5). The thermal efficiency is defined as the thermal differences between the actual state and the reference state, with a relatively larger amplitude over tropical and polar regions in the upper troposphere dominated by the meridional term (Fig. S5) in accordance with the pattern of P_L. The heat transport by transient eddies is dominated by the meridional term, which tends to move heat toward polar areas and to smooth out latitudinal temperature gradients, particularly over the storm-track region (Lau and Oort 1982). Decomposition of the divergence of transient eddy heat transport reveals that the main contributions come from the meridional and vertical components (Fig. S6), bringing heat toward high latitudes and the upper troposphere, respectively. As marginal variation is found in different years, all the decomposition terms in the supplemental figures use the year 1979 data as an example. Although the heat transport divergence by transient disturbances peaks near the surface and at 300 hPa, the $C(P_L, P_H)$ maxima are only around 300 hPa (Fig. 2f) depending on the product of thermal efficiency and heat transport divergence by transient eddies.

The climatological global-mean value of $C(K_L, P_L)$ is -1.58 W m^{-2} (Fig. 2c) in contrast to previous estimates with a minor magnitude and inconclusive sign using the classic LEC due to the canceling effect between the Hadley and Ferrell cells (Li et al. 2007). This highlights the important role of low-frequency waves in transforming P_L to K_L, which is not considered in the zonal-mean component of LEC. Furthermore, the pattern of $C(K_L, P_L)$ mostly reflects the overturning of the thermally direct circulation, while the Ferrel cell plays a dominant role in the LEC (Li et al. 2007). Another possible reason partly accounting for the differences could be large negative anomalies near the surface around the South Pole (Fig. 2g), which are mainly attributed to the strong downward motion there associated with high and complex topography (Fig. S7f) or because the separation into eddy and mean components is different. The conversions from K_L to P_L are determined by the product of $\overline{\delta\alpha}$ and $\overline{\omega}$ [see Eq. (5)]. The symbol δ represents differences between the actual state and the global-mean reference state. The term $\overline{\delta\alpha}$ shows a tripolar pattern with positive anomalies over the tropics and negative anomalies residing on the northern and southern sides (Fig. S7e). The horizontal distribution of $C(K_L, P_L)$ bears a similar pattern to $\overline{\omega}$ (Fig. 2c and Fig. S7c), displaying the same sign over the tropics and the opposite sign to the poleward sides. Strong interactions between K_L and P_L are mainly located over the tropical and polar regions, where a thermally direct circulation dominates. Not surprisingly, relatively weak conversion appears in the midlatitudes where transient eddy processes play a more important role. The tropical anomalies clearly exhibit a similar distribution to the climatological precipitation, such as the intertropical convergence zone structure

and the Pacific dipole associated with the Walker circulations. A possible physical interpretation of this is that the strong negative anomalies over the tropical Indo-Pacific and western Atlantic regions and associated surrounding positive anomalies over the subtropics and eastern Pacific are associated with the conversion of P_L to K_L, which likely supports the maintenance of the Hadley and Walker circulations. This conversion process is mainly characterized by the descent of cold and heavy air and the ascent of warm and light air. Analogously, near the poles, the decrease in P_L contributes to downward motion and sustains the polar cell. The latitude–pressure distribution of $C(K_L, P_L)$ also resembles that of the vertical velocity, with maxima in the mid–upper troposphere over the tropics and near the surface at the poles (Figs. 2g and 6f). In the midlatitudes, positive anomalies are present over the oceans, while negative anomalies are shown over land, particularly over the Pacific sector, which are associated with the thermally indirect circulation due to low-frequency eddy motions (Fig. 2c).

The $C(K_L, P_L)$ and diabatic generation terms are the dominant contribution terms in the P_L budget (Figs. 2c,d). The opposite sign between them indicates that the major part of the P_L generation term is mostly consumed by conversion into low-frequency kinetic energy by $C(K_L, P_L)$, particularly in the tropics. The generation term is mainly contributed by $\tilde{\gamma}\overline{Q}$, while $-\tilde{\chi}$ plays a marginal role, suggesting that the reference state is not highly time dependent. Thus, P_L will be created where the thermal efficiency and diabatic forcing are positively correlated primarily over the equatorial and polar regions and vice versa will be dissipated in midlatitudes. In contrast to Novak and Tailleux (2018), who calculate the diabatic term as a residual of the budget equation, we estimate the diabatic heating term Q explicitly according to the thermodynamic equation as the total derivative of potential temperature. In this sense, our well-closed budget for P_L further demonstrates the validity of the local energetic framework. Figure S8 shows a comparison of diabatic heating (year 1979 as an example) between our diagnostic and ERA5 reanalysis. This comparison shows marginal sensitivity to the year we choose. Patterns and magnitudes both agree with each other quite well albeit with discrepancies particularly in the lower atmosphere. These differences may come from either numerical errors or subdaily processes in ERA5 associated with the diurnal cycle which are not considered in our daily estimates. The latitude–pressure distribution of the diabatic heating rate is characterized by heating in the southern deep tropics and cooling in the northern deep tropics and polar regions (Fig. S9e), which are likely induced by latent heat release and longwave radiative cooling, respectively (Figs. S9f,h). The positive maxima near the surface in the Northern Hemisphere are mainly located over the storm-track region (Fig. S9e), which may be associated with diabatic heating due to strong boundary mixing and latent heat release. Given the distribution of the thermal efficiency (Fig. S5), the diabatic heating over the southern deep tropics and cooling over the northern deep tropics result in APE increases and decreases, respectively (Fig. 2h). This is because the tropics are warmer than other latitudes so that the tropical warming and cooling anomalies increase and decrease the integrated buoyancy force for air parcels to reach the reference state. The spatial distribution of $G(P_L)$ bears a similar structure as mean precipitation suggesting an important role of diabatic heating in generating P_L (Schneider et al. 2014). This also suggests that the precipitation associated with the ITCZ is a major energy source of P_L. By contrast, the polar regions are relatively cooler; therefore, the longwave diabatic cooling raises local temperature departures from the reference state on isobaric surfaces and subsequently contributes to increases in integrated buoyancy force and local APE (Fig. 2h). As the thermal efficiency is of much larger magnitude in the mid–upper troposphere than in the lower atmosphere, the diabatic generation term tends to be stronger aloft, although diabatic heating is strong near the surface in the storm-track region.

c. Climatology of high-frequency APE budget terms

As discussed above, the low-frequency APE is the major source for high-frequency APE through eddy mixing across strong temperature gradients at 300 hPa (Figs. 3c,h). The conversions from low-frequency to high-frequency APEs $C(P_L, P_H)$ and from high-frequency APE to KE $C(K_H, P_H)$ constitute the two most important terms for the P_H budget analysis and largely compensate each other (Figs. 3c,d,h,i), which is in agreement with the classic LEC framework. The $C(P_L, P_H)$ and $C(K_H, P_H)$ terms are maximized poleward of and at the location of the storm-track entrance regions, respectively. The centers of $C(K_H, P_H)$ are shifted downward at about 400 hPa below those of $C(P_L, P_H)$ in the vertical dimension (Figs. 3h,i). This vertical mismatch of centers between two conversions is mainly transformed by the eddy advection term of Eq. (6) (i.e., $-\overline{\mathbf{V}' \cdot \nabla P_T'}$). The total APE P_T is mostly advected equatorward and downward at the entrance of the storm track by transient eddies, leading to decreases and increases in the northern and southern flanks of the eddy APE centers, respectively (Fig. 3b). Subsequently, these increases in P_H are converted into K_H, with a secondary replenishment of P_H due to the generation term $G(P_H)$. The peaks of the standard deviation of $C(K_H, P_H)$ are well collocated with their maxima, indicating that the variations are primarily in intensity on the interannual scale. The term $G(P_H)$ is mostly contributed by $\overline{\gamma' Q'}$ as the $\overline{\gamma}\,\overline{Q}$ and $\tilde{\gamma}\overline{Q}$ terms contribute almost equally and compensate each other. The sensible and latent heat released from eddy processes within the storm-track regions increases P_H. Compared to the P_L generation term, P_H generated due to diabatic heating is much smaller in magnitude, pointing to the driving role of diabatic heating anomalies in generating APE associated with thermally direct circulation systems (e.g., Hadley, Walker, and polar cells). The advection by the low-frequency flow is relatively weaker than other budget terms (Figs. 3a,f), which is only one-fifth in the amplitude of the advection term by transient eddies. Note a different color scale is used. It features a zonal structure over the northern Pacific and Atlantic (Fig. 3a), characterized by negative and positive values in the entrance and exit regions of jet stream. Positive and negative values are situated on the eastern and western sides of P_H centers, respectively, revealing a downstream advection of P_H by the low-frequency flow.

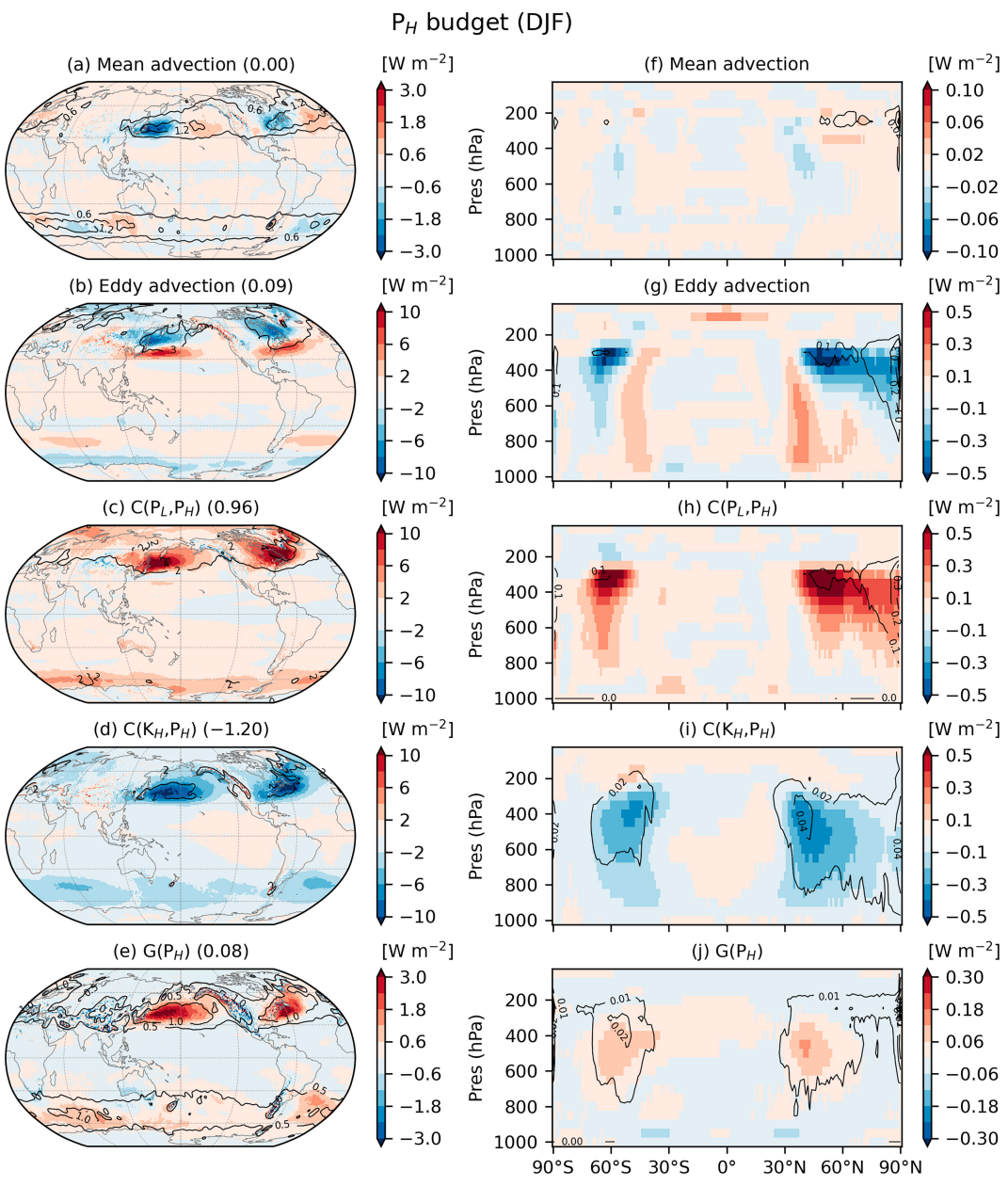

FIG. 3. The distribution of climatological budget terms for high-frequency APE (W m^{-2}). Vertically integrated (1000–50 hPa; mass-weighted) (a) mean advection (shading), (b) eddy advection of high-frequency total APE, (c) conversion from low-frequency to high-frequency APEs $C(P_L, P_H)$, (d) conversion from high-frequency KE to APE $C(K_H, P_H)$, and (e) generation of high-frequency APE $G(P_H)$ in the boreal winter (December–February) during 1980–2021. (f)–(j) As in (a)–(e), but for zonal averages over the globe. The values in parentheses represent the global mean of conversion terms. The contours denote the annual standard deviation.

d. Climatology of high-frequency KE budget terms

The midtropospheric K_H between 900 and 300 hPa is mainly converted from P_H over the upstream part of the storm-track regions in the Northern Hemisphere as discussed in the previous section (Figs. 4b,g). Most of K_H is consumed by $-\overline{\mathbf{V}'\cdot\nabla\delta\Phi'}$ (i.e., advection of high-frequency geopotential anomalies with respect to the reference state by transient eddies; Fig. 4g), which represents the pressure work term associated with eddies (Orlanski and Katzfey 1991). Further decomposition of $-\overline{\mathbf{V}'\cdot\nabla\delta\Phi'}$ into different components shows that the midtropospheric negative anomalies are mainly contributed by the vertical component, suggesting a downward transport of geopotential (Figs. S10c,f). The zonal and meridional components largely offset each other above 900 hPa but have a synergistic effect in generating K_H in the lower troposphere (Figs. S10a,b,d,e). In the upper troposphere, the overwhelming effect of positive anomalies due to the meridional advection results in increases in K_H in the midlatitudes

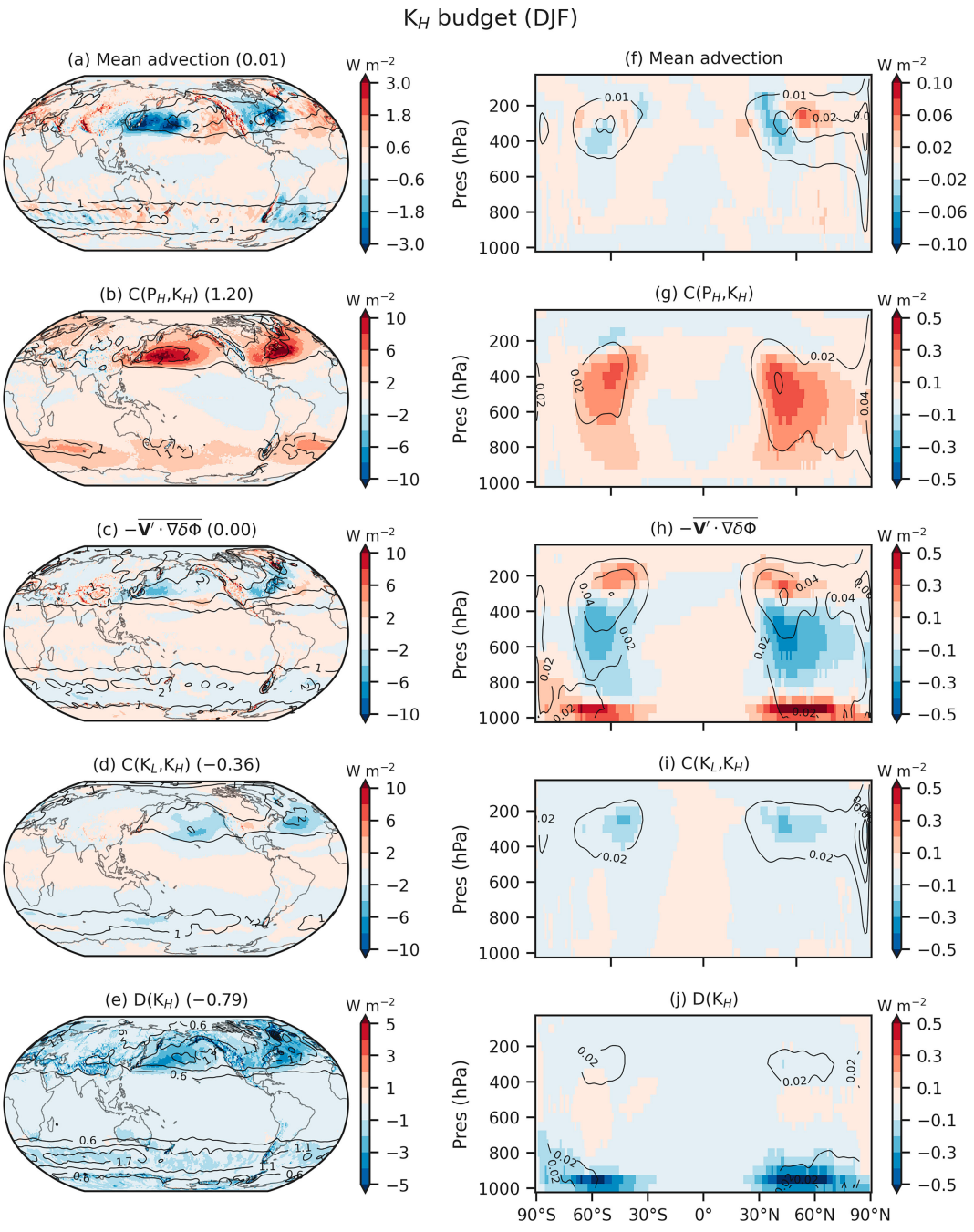

FIG. 4. The distribution of climatological budget terms for high-frequency KE (W m^{-2}). Vertically integrated (1000–50 hPa; mass-weighted) (a) mean advection (shading), (b) conversion from high-frequency APE to KE $C(P_H, K_H)$, (c) low-frequency eddy advection of high-frequency geopotential anomaly with respect to reference state $-\mathbf{V}'\cdot\nabla\delta\Phi'$, (d) conversion from low-frequency to high-frequency KEs $C(K_L, K_H)$, and (e) dissipation of high-frequency KE $D(K_H)$ in the boreal winter (December–February) during 1980–2021. (f)–(j) As in (a)–(e), but for zonal averages over the globe. The values in parentheses represent the global mean of conversion terms. The contours denote the annual standard deviation. The term $\mathbf{V}$ represents three-dimensional wind including both horizontal and vertical components.

(Fig. 4h). This increased K_H is later converted into K_L located at the end of the storm-track region, where barotropic processes dominate associated with momentum convergences in the upper troposphere to maintain the jet stream (Figs. 4d,i). The dominant sink term for K_H is dissipation through friction, mainly located in the storm-track region within the planetary boundary layer (Figs. 4e,j). The pattern of $-\overline{\mathbf{V}}\cdot\nabla K_H$ (advection of high-frequency kinetic energy) is characterized by negative and positive values to

the west and to the east of the K_H center, respectively, over the northern Pacific and Atlantic (Fig. 4a). This may suggest the role of downstream K_H advection by the low-frequency flow in the life cycle of a baroclinic disturbance. A dipole pattern contribution is seen in the upper troposphere in the rotation term, with negative values over the midlatitudes and relatively weaker positive values to the north (Figs. S11c,f). This metric term is mainly contributed by the tangent term of the spherical term $-[(\overline{u}\overline{u'v'} - \overline{v}\overline{u'u'})/a]\tan\phi$ (not shown) in Eq. (10).

e. Climatology of low-frequency KE budget terms

Analogously to the K_H budget, $C(P_L, K_L)$ is mostly compensated by $-\overline{\mathbf{V}}\cdot\nabla\overline{\delta\Phi}$ (i.e., low-frequency advection of geopotential anomalies) in the tropics and polar regions (Figs. 5h,i), which denotes the effect of work done by the pressure force associated with the low-frequency flow (Holopainen 1978). This low-frequency advection term broadly resembles its vertical component with marked compensation effects between the zonal and meridional components (Fig. S12). Within the storm track, the negative $C(P_L, K_L)$ anomalies suggest an increase in large-scale baroclinicity via the ageostrophic meridional flow (Fig. 5b), which is partially offset by the barotropic conversion from high- to low-frequency KEs at the end of the storm track (Fig. 5d; Novak 2016). Additionally, K_L is generated at the entrance of the jet stream, while being consumed at the end (Fig. 5c), largely opposing the low-frequency advection of K_L (Fig. 5a). This offsetting effect of the latter on the former (i.e., reduction in K_L) is also evident in the zonal mean at 200 hPa between 30° and 60°N (Figs. 5g,i), with secondary supplement from $C(K_H, K_L)$, $D(K_L)$, and $-\nabla\cdot(\overline{\mathbf{V}}_h\,\overline{\mathbf{V}'\mathbf{V}'_h})$ terms (Figs. 5j,k,l). Inspection of the term corresponding to the convergence of the momentum transport by the mean flow $-\nabla\cdot(\overline{\mathbf{V}}_h\,\overline{\mathbf{V}'\mathbf{V}'_h})$ shows a meridional dipole over the northwestern Pacific and Atlantic, with negative and positive values straddling the jet core axis to the south and the north, respectively, suggesting a northward displacement of the jet stream (Figs. 5e,k). This term $-\nabla\cdot(\overline{\mathbf{V}}_h\,\overline{\mathbf{V}'\mathbf{V}'_h})$ is primarily contributed by the component $-\nabla\cdot(\overline{u}\,\overline{\mathbf{V}'u'})$ associated with equivalent barotropic westerly momentum transport of Reynold's stress in the meridional direction $-\nabla\cdot(\overline{u}\,\overline{v'u'})$ (Fig. S13). The sink of K_L is largely due to the dissipation term due to friction within the planetary boundary layer (Figs. 5f,l). Its magnitude is about two times the K_H dissipation. Note that there are discernible positive values of dissipation in K_L over the northeastern Pacific and midlatitudes in the zonal-mean distribution, which could be related to Ekman pumping (Feldstein 2002, 2003).

4. Long-term changes in the atmospheric energetics

In the previous section, we have identified the three-dimensional spatial distribution of climatological features of atmospheric energetics. Now, we proceed to examine their long-term changes, which can help to provide a new perspective for understanding climate change. Figure 6 displays the long-term changes in different energetic forms and associated budget terms averaged over 0°–360°, 60°S–60°N during 1980–2021. The polar region is excluded because of the nonconservation issue of mass and energy there. There is a significant increasing trend of P_H and K_H, suggesting intensified eddy and storm activities, which is consistent with previous studies on historical changes in eddy energetics using reanalysis (Pan et al. 2017; Ma et al. 2021). These prominent increases in P_H and K_H well correspond to the significant increasing trend of the conversion terms, $C(P_L, P_H)$ and $C(P_H, K_H)$, respectively. This finding indicates an increase in baroclinic instability, which mainly occurs in the midlatitudes at the synoptic scale and is associated with the conversion of P_L to P_H and subsequently to K_H (Lembo et al. 2019). The low-frequency energetic forms also show increases but do not reveal any significant long-term changes. It is noteworthy that climate model studies tend to present a suppressed energy cycle in response to a warming scenario (Lucarini et al. 2010; Michaelides 2021; Kanno and Iwasaki 2022). This controversy between observed historical and projected future changes may be because the model cannot replicate the observed atmospheric energy cycles, mostly too vigorous in model simulations as suggested by Boer and Lambert (2008). Revealing the exact reason why there are differences between historical and future changes in energy cycles is out of the scope of our current study. Our work overall agrees with the previous literature using reanalysis, and it may be useful to investigate this controversy from a local perspective in the future. Next, the characteristics of long-term changes in energetics will be explored from a regional view over the boreal winter hemisphere.

a. Long-term changes in APE and KE terms

Figure 7 shows the long-term changes in various energetic forms between two 15-yr time periods (i.e., 2007–21 and 1980–94). We also checked the changes between two 20-yr time periods, which are highly consistent with those presented in the following analysis. There is a prominent decrease in the low-frequency APE over the Arctic (Fig. 7a). This is expected as the temperature over the Arctic increases much faster than that over other regions, a phenomenon referred to as "Arctic amplification" (Serreze et al. 2009). The increases in temperature reduce the departure from the isobaric mean over the Arctic. As a result, the magnitude of differences in pressure between actual state and low-frequency state becomes smaller, characterized by positive anomalies (Fig. S14) in contrast to the negative climatology (Fig. S1). The decreases in differences in $p - \tilde{p}_r$ subsequently reduce APE over the Arctic. Similar to the climatology, stronger changes in P_L appear in the upper troposphere than near the surface resembling the changes in $p - \tilde{p}_r$ despite the pronounced surface Arctic warming. In the midlatitudes, a significant increasing trend is displayed over Siberia in conjunction with a significant cooling trend at layers between 600 and 400 hPa (not shown), increasing the temperature variance locally. This temperature trend pattern has been referred to as the warm Arctic-cold Eurasia pattern (Shepherd 2016) and has been linked to a weakened polar vortex in the Arctic amplification era from 1990 onward (Kretschmer et al. 2018). Subsequently, it leads to changes in stationary wave patterns, storm tracks, and

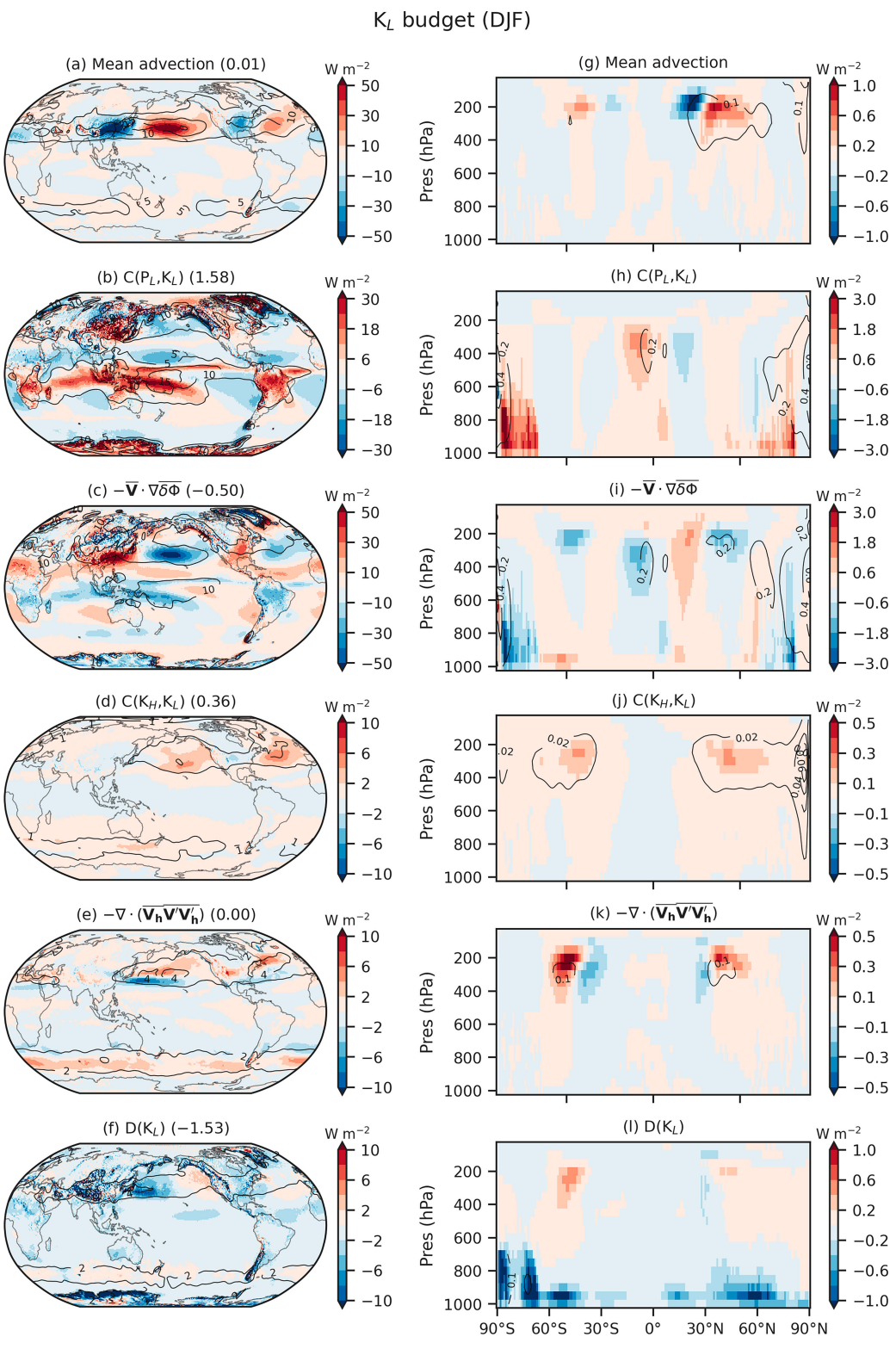

FIG. 5. The distribution of climatological budget terms for low-frequency KE (W m^{-2}). Vertically integrated (1000–50 hPa; mass-weighted) (a) mean advection, (b) conversion from low-frequency APE to KE $C(P_L, K_L)$, (c) mean advection of low-frequency geopotential anomaly with respect to reference state $-\overline{\mathbf{V}}\cdot\nabla\overline{\delta\Phi}$, (d) conversion from high-frequency to low-frequency KEs $C(K_H, K_L)$, (e) convergence of the mean flux of westerly momentum in meridional direction $-\nabla\cdot(\overline{\mathbf{V}}_h\,\overline{\mathbf{V}'\mathbf{V}'_h})$, and (f) dissipation of low-frequency KE $D(K_L)$ in the boreal winter (December–February) during 1980–2021. (g)–(l) As in (a)–(e), but for zonal averages over the globe. The values in parentheses represent the global mean of conversion terms. The contours denote the annual standard deviation. The term $\mathbf{V}$ represents three-dimensional wind including both horizontal and vertical components. The term $\mathbf{V}_h$ denotes horizontal wind.

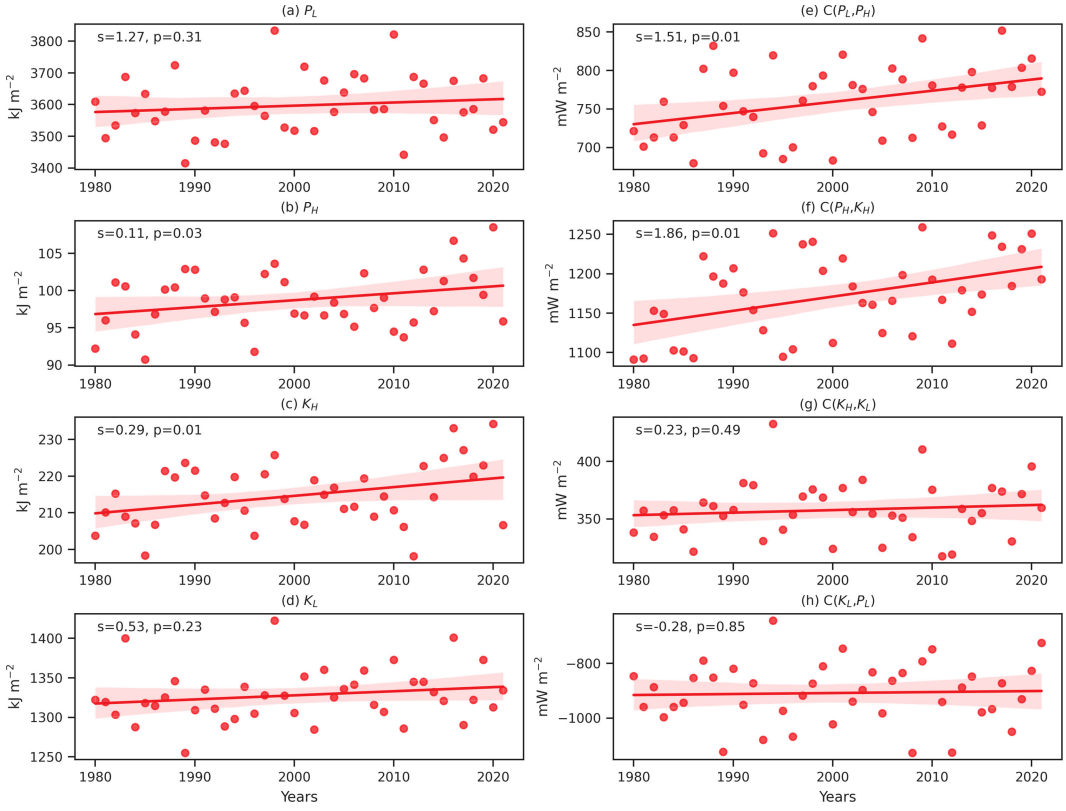

FIG. 6. Time series of different energetic (kJ m^{-2}) and associated conversion (mW m^{-2}) terms in winter averaged over 0°–360°, 60°S–60°N during 1980–2021. (a) P_L, (b) P_H, (c) K_H, (d) K_L, (e) $C(P_L, P_H)$, (f) $C(P_H, K_H)$, (g) $C(K_H, K_L)$, and (h) $C(K_L, P_L)$. The polar regions are excluded because mass and energy are not conserved there in the ERA5 reanalysis. The straight line indicates the linear trend. Slope and significance levels are denoted by s and p values, respectively, in the upper-left corner of each panel. The red shading denotes the 95% confidence interval of the fitted line.

associated jets (Simpson et al. 2016; Coumou et al. 2018). In the downstream area, there is a dipolar trend of P_H over the northern Pacific, with positive and negative anomalies on the northern and southern flanks of the climatological maxima, respectively, suggesting a northward displacement of the P_H center (Fig. 7b). This increasing trend of P_H is located slightly southward and downward of that of P_L, similar to their climatological structure (Figs. 7e,f), which may indicate a strengthened conversion from P_L to P_H. Another important feature of the P_H trend is characterized by a homogeneous increase over the tropics throughout the troposphere. These increases coincide well with the upward trend of K_H (Figs. 7c,g), indicating increases in synoptic disturbances under global warming. To the north over the northern Pacific, there is a dipole of trends in K_H at 300 hPa, resembling that of P_H but slightly shifted toward the downstream region and showing a northward shift of storm tracks over the Pacific (Wang et al. 2017). This means a northward shift of the storm tracks possibly related to conversions from P_H to K_H. In addition, the dipolar structure of the K_H trend is situated to the northeast of the K_L trend with a similar polarity (Fig. 7d). The jets thus can gain and lose more energy at the entrance of the northern and southern flanks of the storm tracks, respectively, highlighting the role of conversion from K_H to K_L in the northward shift of the jet stream over the Pacific. Such a northward shift of the jet stream is also reported in Simmons (2022). This shift of storm tracks and jet streams has been found closely linked to the variations in the location or intensity of extreme weather events in the midlatitudes including coastal flooding (Colle et al. 2008), heatwaves (Chang et al. 2016), and wildfire activity (Dannenberg and Wise 2017). Interestingly, the associated energetic changes are much weaker or insignificant over the Atlantic than in the Pacific. This zonal asymmetry has also been reported in previous studies (Wang et al. 2017; Oudar et al. 2020; Priestley and Catto 2022). For instance, Wang et al. (2017) revealed a weakening of the storm track over the North Atlantic and a poleward displacement over the North Pacific during 1979–2015 and attributed these changes to the baroclinic energy conversion changes associated with eddy–mean flow interactions as a result of the weaker meridional gradients. In the following section, we will examine variations in the conversion terms, which can enable us to gain a better and comprehensive understanding of the regional energetic form changes.

b. *Low-frequency APE budget changes*

The long-term changes in the budget terms are examined to delineate how the contribution of different conversion terms

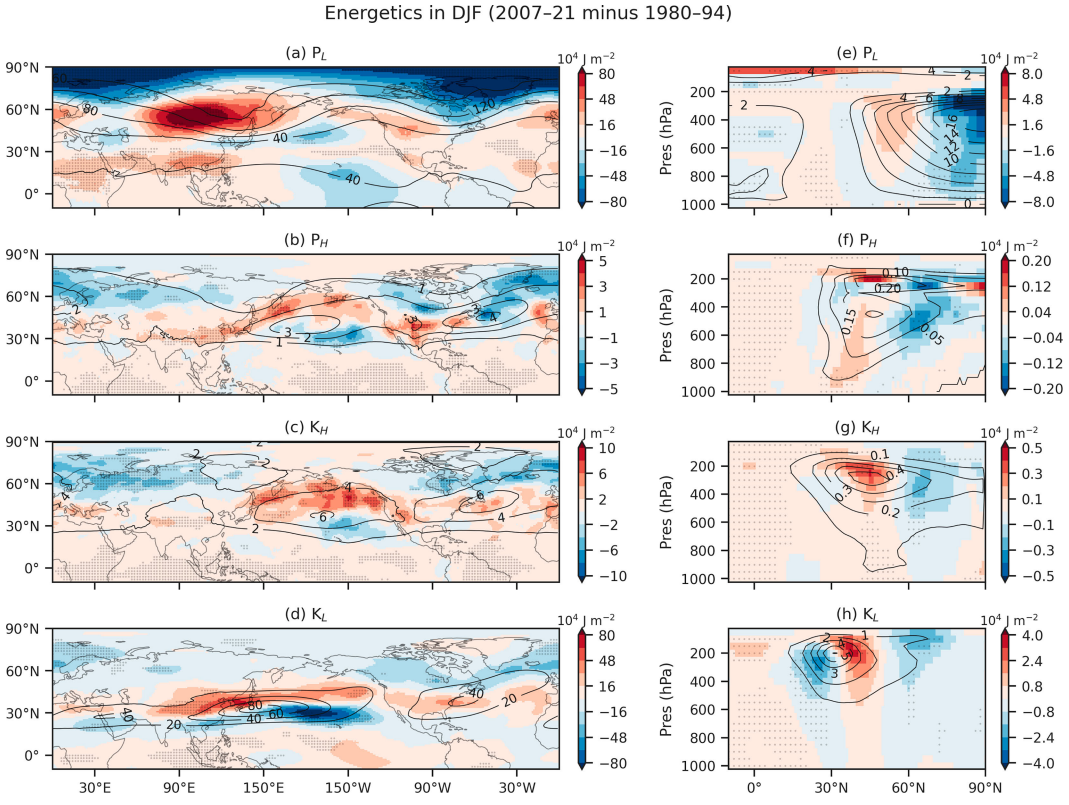

FIG. 7. The long-term changes (10^4 J m^{-2}) in energetic terms in the boreal winter (December–February) during 1980–2021. (a) Low-frequency APE, (b) high-frequency APE, (c) high-frequency KE, and (d) low-frequency KE. Black dots mark the grid points where the changes are at the 0.05 significance level according to the Student's *t* test. (e)–(h) As in (a)–(d), but for zonal averages over the globe.

varies between the two time periods. The long-term changes in P_L mean advection feature an increased band from northeastern China to Japan and the adjacent ocean in conjunction with its climatological extrema (Figs. 8a and 2a). The latitude–pressure cross section of changes shows a dipole in the mid–upper troposphere between 500 and 300 hPa, with negative values between 50°N and the North Pole and positive values between 40° and 50°N (Fig. 8b). This pattern is generally consistent with the climatological mean advection, indicating a stronger meridional advection from the polar region toward the midlatitudes. Albeit significant, the changes over the tropics tend to be fragmentized. There is a dipolar pattern of zonal-mean changes in $C(P_H, P_L)$ over the high latitudes between 600 and 400 hPa (Fig. 8f). This dipole resides on the northern and southern sides of its climatological negative center, suggesting a southward displacement of the conversion extrema. Interestingly, further checking the distribution of $C(P_H, P_L)$ dipole changes is characterized by a contrasting response over the two storm tracks, with decreases from northeastern China to Japan and increases from the northeastern United States to the Atlantic (Fig. 8b). These conversion anomalies serve as a compensation effect to the mean advection term (Figs. 8a,b). For the $C(K_L, P_L)$ term, the changes mainly appear in the tropical and polar regions, particularly in the former (Figs. 8c,g). There are negative anomalies over the eastern equatorial Pacific and the Maritime Continent extending southeastwardly (Fig. 8c), accompanied by anomalous upward motion of warm air converting P_L to K_L. Between these negative anomalies, positive anomalies are seen over the western and southeastern Pacific associated with anomalous downward motion of warm air transforming K_L into P_L. This dipolar pattern of anomalies over the western and central Pacific agrees with a strengthening and westward shift of the Pacific Walker circulation in recent decades (Sohn and Park 2010; Takahashi and Watanabe 2016), which probably arises from the internal climate variability (Bordbar et al. 2017; Chung et al. 2019) such as the warming of the Atlantic (McGregor et al. 2014) and phases of the interdecadal Pacific oscillation (England et al. 2014). The zonal-mean long-term changes are also characterized by a dipole within the northern tropics with decreases and increases over the northern and southern parts, respectively (Fig. 8g), in favor of a northward shift of the ascending branch of the Hadley circulation. To the north, the positive anomalies denote a strengthening of the descending branch of the Hadley cell due to stronger conversions into P_L from K_L. Changes in the P_L generation term exhibit a reversed dipole as compared to $C(K_L, P_L)$ over the tropics, compensating with each other (Figs. 8d,h). The increases and decreases in the generation term are mainly related to the changes in latent heat release associated with the

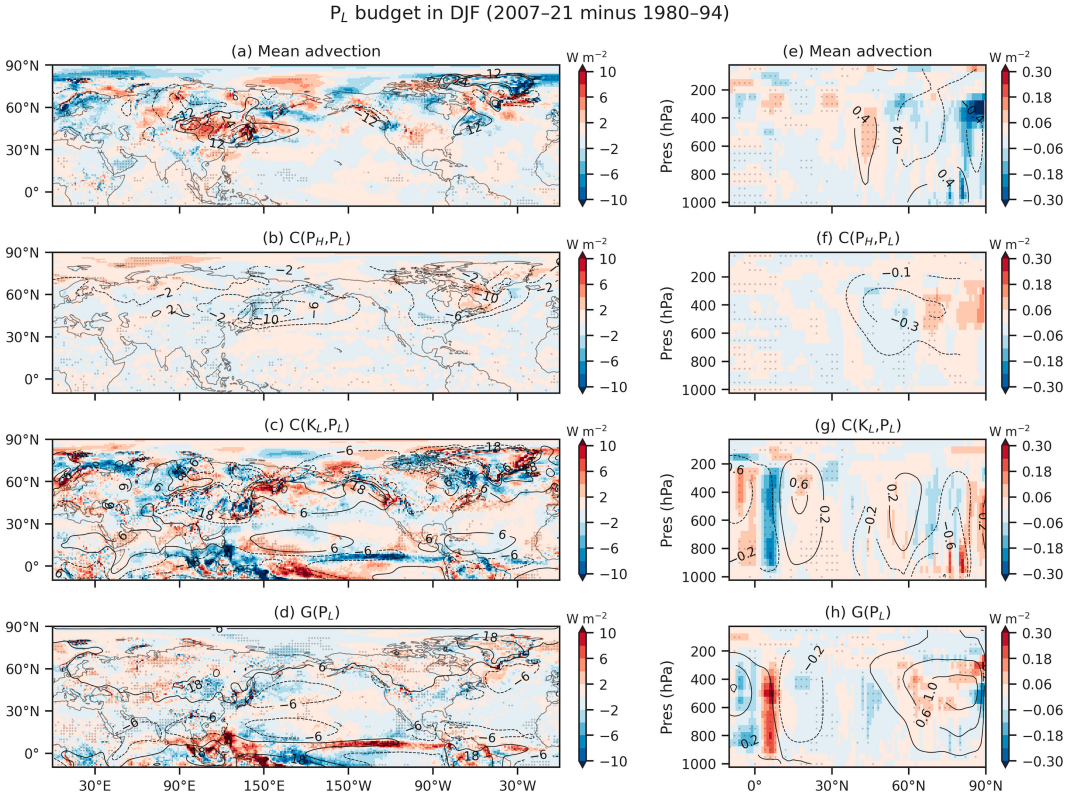

FIG. 8. The long-term changes in the budget of low-frequency APE budget (W m^{-2}) in the boreal winter (December–February) between 2007–21 and 1980–94. (a) Mean advection (shading), (b) conversion from high-frequency to low-frequency APEs $C(P_H, P_L)$, (c) conversion from low-frequency KE to APE $C(K_L, P_L)$, and (d) generation of low-frequency APE $G(P_L)$ in the boreal winter (December–February) during 1980–2021. (e)–(h) As in (a)–(d), but for zonal averages over the globe. Black dots mark the grid points where the differences are at the 0.05 significance level according to the two-sided Student's t test. The contours denote the long-term climatology during 1980–2021.

potential temperature changes. Although the contribution from different budget balances may vary between the two periods, their offsetting effects result in minor changes in the tendency of P_L (Figs. S15a,d).

c. *High-frequency APE budget changes*

Most of the P_H budget term changes appear in eddy advection, $C(P_L, P_H)$, and $C(K_H, P_H)$, while relatively marginal differences are shown in the mean advection and the generation terms. Note that the differences in $C(P_L, P_H)$ play an important role in the P_H budget changes, but not for the P_L budget changes. This is expected as $C(P_L, P_H)$ is the main source of P_H (Fig. 3). The spatial distribution of integrated eddy advection changes displays a wave-like pattern with alternating positive and negative anomalies within the same latitude band (Fig. 9b). The latitude–pressure cross section of eddy advection changes is characterized by a meridional dipole structure in the midtroposphere with positive anomalies over the North Pole and negative anomalies in the midlatitudes (Fig. 9g), suggesting a northward transport of P_H by high-frequency eddies. The positive anomalies of P_H over the polar regions are mainly transferred into P_L (Fig. 9h), with a secondary contribution from $C(K_H, P_H)$ (Fig. 9i). The negative counterpart in the midlatitudes is mostly replenished by P_L (Fig. 9h).

d. *High-frequency KE budget changes*

The major changes in the K_H budget come from $C(P_H, K_H)$, the low-frequency eddy advection of high-frequency geopotential anomaly $-\overline{\mathbf{V}' \cdot \nabla \delta\Phi'}$, and the dissipation terms (Fig. 10). Positive anomalies are present over the storm-track regions where the strongest $C(P_H, K_H)$ occurs, suggesting more P_H converting into K_H in the later period (Fig. 10b). To the north, negative anomalies are seen, particularly over the northwestern Atlantic and Greenland. The cross section is thus characterized by a dipolar pattern in the mid–upper troposphere, with positive and negative anomalies in the mid- and high latitudes, respectively (Fig. 10g). The changes in $-\overline{\mathbf{V}' \cdot \nabla \delta\Phi'}$ exhibit a similar pattern compared to those in $C(P_H, K_H)$ but reversed polarity, indicating their largely compensating effects (Figs. 10c,h). Additionally, there is another dipolar pattern of anomalies in $-\overline{\mathbf{V}' \cdot \nabla \delta\Phi'}$ in the lower atmosphere, with positive anomalies in the midlatitudes and negative anomalies in the high latitudes, showing a quadrupole pattern in the zonal-mean distribution (Fig. 10h). These anomalies are mostly offset by the changes in the dissipation term (Fig. 10j). The decreases in the dissipation in the atmosphere over the

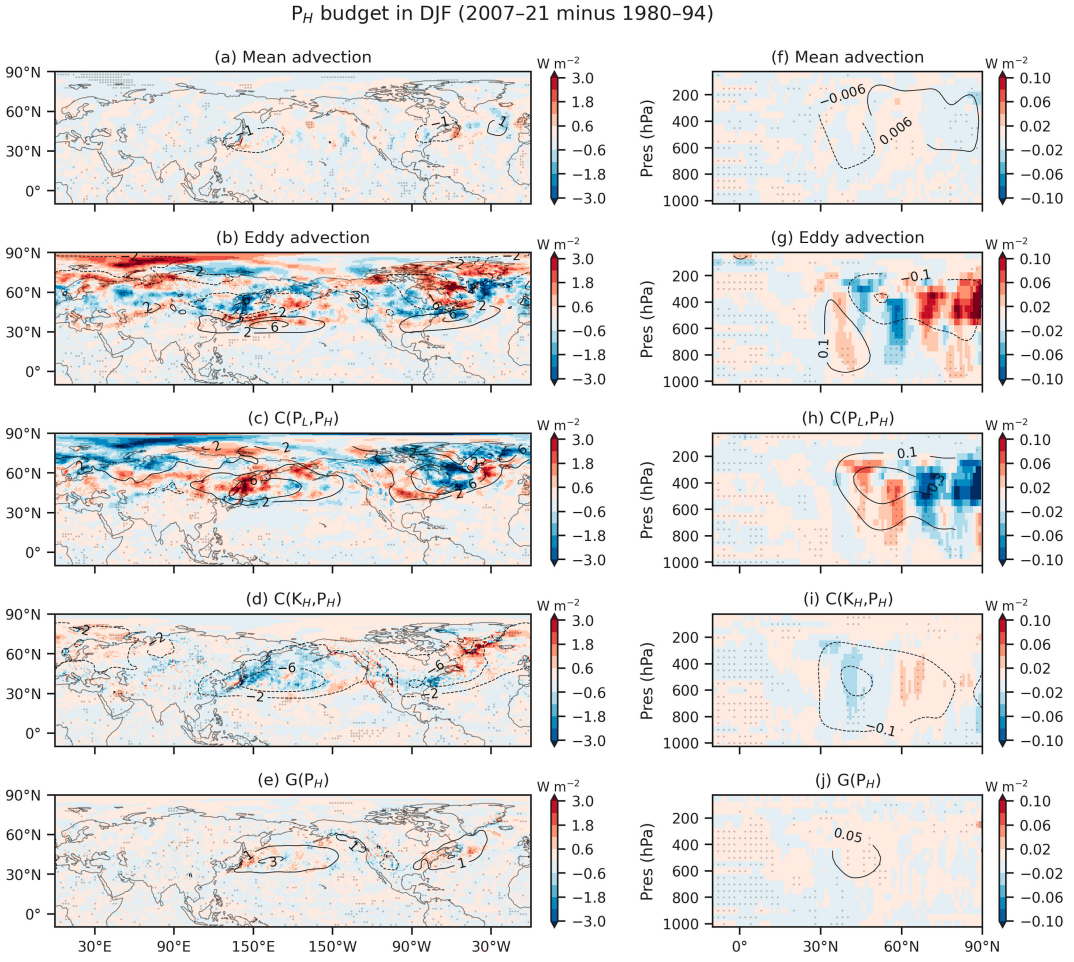

FIG. 9. The long-term changes in the budget of high-frequency APE budget (W m^{-2}) in the boreal winter (December–February) between 2007–21 and 1980–94. (a) Mean advection (shading), (b) eddy advection, (c) conversion from low-frequency to high-frequency APEs $C(P_L, P_H)$, (d) conversion from high-frequency KE to APE $C(K_H, P_H)$, and (e) generation of high-frequency APE $G(P_H)$. (f)–(j) As in (a)–(e), but for zonal averages over the globe. The contours denote the long-term climatology during 1980–2021.

tropics indicate an intensified dissipation in the later period (2007–21). This may be related to the increases in the K_H there (Figs. 7c,g).

e. *Low-frequency KE budget changes*

The major changes in the K_L budget are the mean advection, $C(P_L, K_L)$, and the mean advection of the low-frequency geopotential anomaly, while $C(K_H, K_L)$, the convergence of momentum fluxes, and dissipation play a relatively minor role (Fig. 11). The changes in mean advection display alternating positive and negative anomalies in the midlatitudes, particularly over the Pacific (Fig. 11a). A prominent zonal dipolar pattern of anomalies is present with increases and decreases over the western and eastern Pacific, respectively. This pattern opposes the climatological mean advection with their centers shifted eastward, suggesting a weakening of the mean advection. However, a reversed dipole is displayed in the geopotential anomaly advection changes, compensating the mean advection impact (Fig. 11c). Over the tropics and poles, stronger anomalies are found in the $C(P_L, K_L)$ and the geopotential anomaly advection term, offsetting with each other (Figs. 11b,c,h,i). These counteracting effects, among different terms, result in small changes in the local tendency (Figs. S16a,b).

5. Summary and discussion

In this study, the boreal winter climatology and long-term changes in various energetic forms and their associated budget terms in the Northern Hemisphere are presented using ERA5 reanalysis data in the context of a local energetic framework (Novak and Tailleux 2018). The main advantage of this local energetic framework is to provide the local information of APE and its interactions with KE as compared to the classic Lorenz energy cycle. A further decomposition of various energetic forms into low- and high-frequency components enables us to further understand the spatial variations

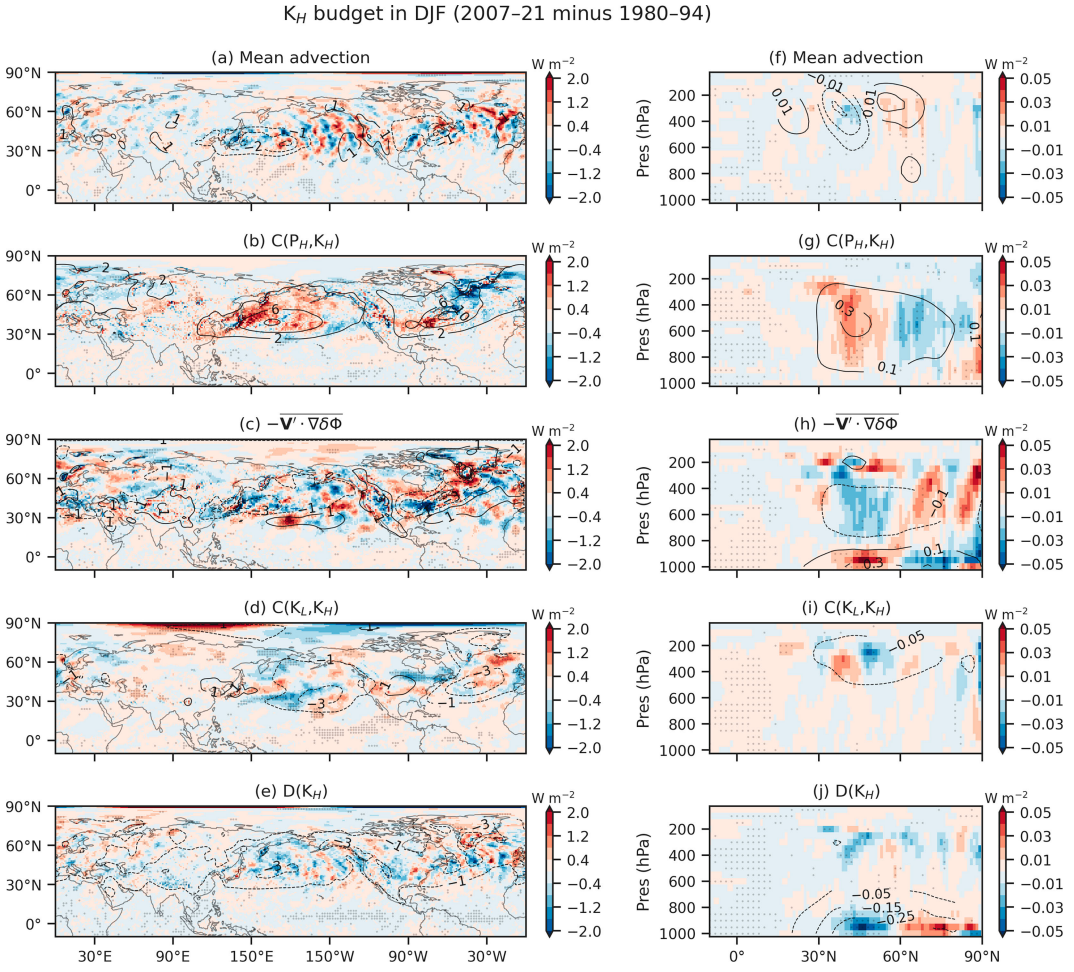

FIG. 10. The long-term changes in the budget of high-frequency KE budget (W m^{-2}) in the boreal winter (December–February) between 2007–21 and 1980–94. (a) Mean advection (shading), (b) conversion from high-frequency APE to KE $C(P_H, K_H)$, (c) low-frequency eddy advection of high-frequency geopotential anomaly with respect to reference state $-\overline{\mathbf{V}'\cdot\nabla\delta\Phi'}$, (d) conversion from low-frequency to high-frequency KEs $C(K_L, K_H)$, and (e) dissipation of high-frequency KE $D(K_H)$. (f)–(j) As in (a)–(e), but for zonal averages over the globe. The contours denote the long-term climatology during 1980–2021.

of the conversions between APE and KE in contrast to the traditional zonal-mean and eddy partitioning.

The extrema of low-frequency APE are mainly located over the poles and the tropics in the midtroposphere, where the largest departure relative to the reference state pressure occurs. The high-frequency APE is mostly concentrated in the midlatitudes peaking downstream and to the south of the low-frequency APE centers in agreement with strong eddy activity there. Two maxima are shown vertically at 500 and 200 hPa. The centers of low-frequency KE are located over the Pacific and the Atlantic at 300 hPa, while those of high-frequency KE are situated to the northeast, corresponding to the locations of the jet streams and storm tracks, respectively. The well-collocated locations of APE, KE, and their conversions may further support the rationale of this local view of atmospheric energetics. For example, P_H, K_H, and $C(P_H, K_H)$ all have a peak of around 400 hPa in the midlatitudes of the Northern Hemisphere. By contrast, this feature is not apparent from the zonal-mean distribution of classic Lorenz energy cycle (e.g., Li et al. 2007), which assumes that the globally integrated energetics can also be interpreted in a local sense.

Low-frequency APE is mainly generated over the tropics and the poles and consumed in the midlatitudes being converted into eddy APE, which is subsequently transformed into high-frequency KE. Both conversions are baroclinic processes, and while the former is mainly related to diabatic heating anomalies at 500 hPa associated with the thermally direct circulation, the latter is mostly guided by horizontal heat transport by transient eddies at 300 hPa. Globally, part of the high-frequency KE is converted into low-frequency KE, involving barotropic processes, and the remainder is dissipated due to friction within the planetary boundary layer. This energy pathway of low-frequency APE → high-frequency APE → high-frequency KE → low-frequency KE overall is consistent with the classic LEC four-box model (e.g., Ma et al. 2021). However, our local framework provides a much clearer picture of the compensation

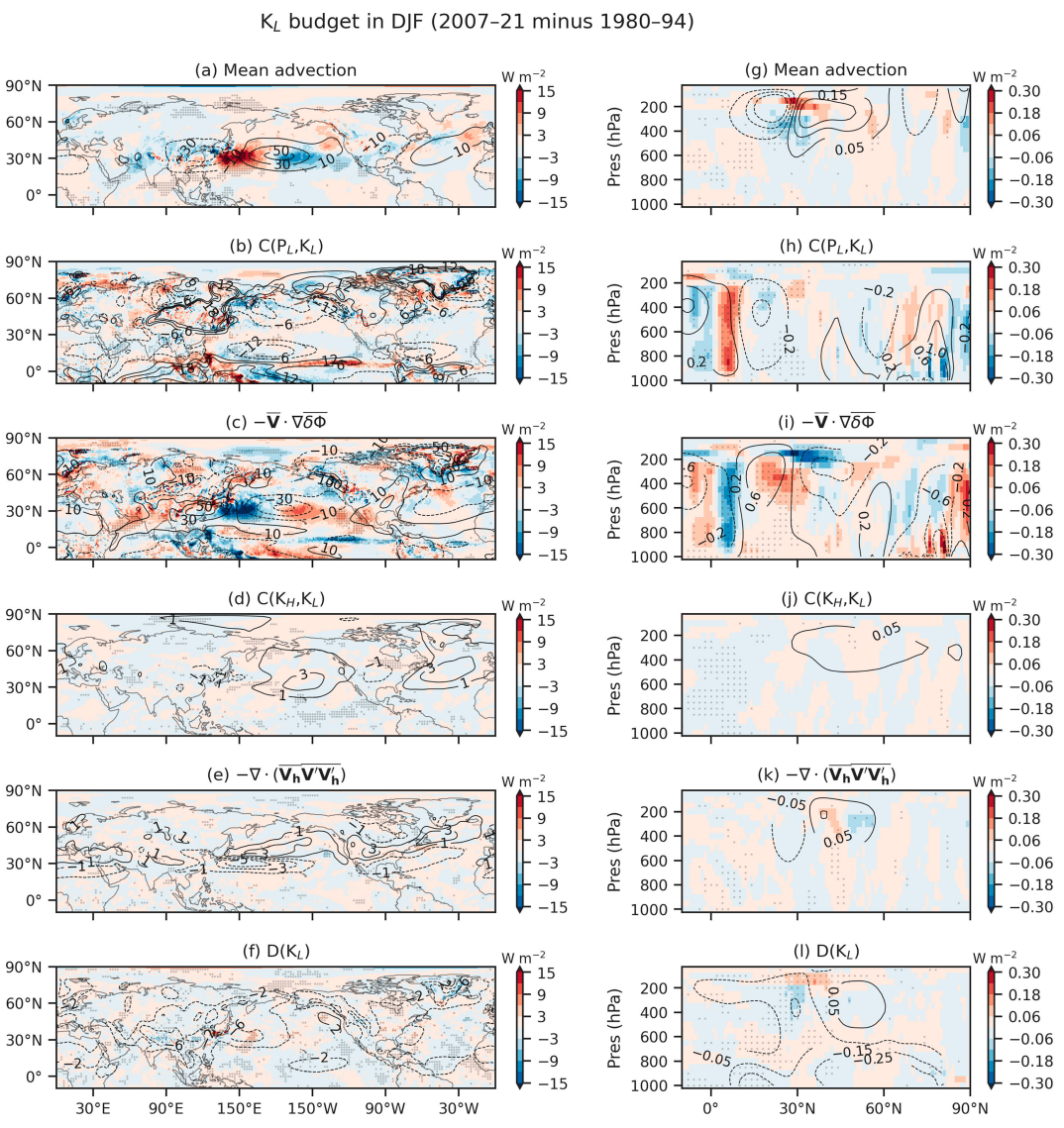

FIG. 11. The long-term changes in the budget of low-frequency KE budget (W m^{-2}) in the boreal winter (December–February) between 2007–21 and 1980–94. (a) Mean advection, (b) conversion from low-frequency APE to KE $C(P_L, K_L)$, (c) mean advection of low-frequency geopotential anomaly with respect to reference state $-\overline{\mathbf{V}}\cdot\nabla\overline{\delta\Phi}$, (d) conversion from high-frequency to low-frequency KEs $C(K_H, K_L)$, (e) convergence of the mean flux of westerly momentum in meridional direction $-\nabla\cdot(\overline{\mathbf{V}}_h\overline{\mathbf{V}'\mathbf{V}'_h})$, and (f) dissipation of low-frequency KE $D(K_L)$. (g)–(l) As in (a)–(f), but for zonal averages over the globe.

effects at regional scales among the different terms. For instance, the conversion from high-frequency APE to KE is largely offset by the eddy advection term of total APE. The conversion from high-frequency APE to KE is mainly counteracted by low-frequency eddy advection of high-frequency geopotential anomaly $-\overline{\mathbf{V}'\cdot\nabla\delta\Phi'}$. Another notable difference between this local framework and the classic LEC is the conversion term from low-frequency APE to KE. This term mainly reflects the overturning of the thermally direct circulation in the former but displays a comparatively minor magnitude and inconclusive sign in the latter, in which the Ferrel cell dominates. Moreover, we found that the globally integrated mean advection of low-frequency APE is not zero, particularly over Greenland and Antarctica associated with complex terrain, which is mainly because the mass and energy are not conserved in ERA5 reanalysis due to data assimilation. This means that the globally integrated budget assessed using reanalysis may not be reliable, a limitation that applies to the classic LEC but that has remained unnoticed so far due to the hidden nature of advection in the global APE framework. While such errors also affect the local framework, the regional changes can still be separated from the erroneous regions. It indirectly underscores the importance of examining the energetics from a local perspective.

The long-term changes in the low-frequency APE are characterized by a dipole at 400 hPa in the Northern Hemisphere, with decreases over the pole and increases over Siberia. This dipole shifts southwestward over the northern Pacific in the high-frequency APE changes at 500 hPa and in the high-frequency KE trend at 300 hPa, where their climatological extrema peak. These increases are well collocated with their centers, while decreases are to the north of the centers, suggesting a strengthening and narrowing of the synoptic eddy activities. This is in stark contrast with Franzke and Harnik (2023), which show an overall weakening of eddy fluxes during 1958–2018 based on the JRA-55 reanalysis. The discrepancies of long-term changes may be caused by the different analyzed periods. Kanno et al. (2016) revealed that the Siberia cooling is much stronger in the later period after 1979 than that starting from 1958. Another possible reason could be related to the circulation uncertainty in different reanalysis products due to a lack of observation in data assimilation, particularly over the ocean (Chemke and Polvani 2020). However, ERA5 reanalysis has been found to be the closest to observations in wind performance among different reanalysis products (Fan et al. 2021; Gualtieri 2022). For the low-frequency KE, there is an anomalous tripolar pattern of trend, with increases in the northern flank of the jet and decreases in the southern flank and to the north of the jet over the Pacific. This means a northward displacement and narrowing of the Pacific jet stream under global warming.

Further analysis of changes in the energetic budget between the periods of 2007–21 and 1980–94 helps to quantify the contribution of different terms in generating the long-term changes in the energetic forms. The zonal-mean changes in $C(P_L,P_H)$ show a dipolar pattern, with negative anomalies in polar regions and positive anomalies in the midlatitudes (Fig. S17e), resembling those of P_L changes. This is likely connected to the stationary wave structure changing and shifting P_L tongues, where the cold air outbreaks associated with conversion to eddies give rise to storm tracks, equatorward over the continents. Interestingly, inspection of spatial distribution of changes in the midlatitudes displays a contrasting difference between the Pacific and the Atlantic (Fig. S17a). The former is characterized by an intensified conversion from P_L to P_H over the northwestern Pacific, while the latter shows a weakening over the northwestern Atlantic. In the downstream regions, these anomalies subsequently result in more conversions to K_H over the Pacific and less over the Atlantic (Fig. S17b). Both $C(P_L, P_H)$ and $C(P_H, K_H)$ are associated with baroclinic processes, suggesting a stronger and weaker baroclinicity over the Pacific and the Atlantic, respectively, consistent with Wang et al. (2017). Further to the east, $C(K_H, K_L)$ is enhanced over the central Pacific and weakened over the Atlantic (Fig. S17c), associated with barotropic processes. These strengthening and weakening conversion processes over the Pacific and the Atlantic indicate an accelerated energy cycle in the former and a suppressed energy cycle in the latter. The changes in $C(P_L, K_L)$ are mainly featured with significant differences in the deep tropical regions, characterized by positive values over the eastern equatorial Pacific and the Maritime Continent and negative anomalies in-between over the western–central Pacific (Fig. S17d). This anomaly pattern coincides with a strengthening and westward shift of the Walker circulation likely arising from the internal climate variability (Chung et al. 2019).

Furthermore, the low-frequency APE changes in the boreal midlatitudes over East Asia are predominantly driven by an enhanced mean advection and are subsequently consumed by conversion into high-frequency APE. As a result, the high-frequency APE increases in the downstream areas. However, this intensification is mainly compensated by eddy advection rather than conversion into high-frequency kinetic energy, depicting a more complete picture than the classic paradigm. Changes in the high-frequency KE are mainly induced by conversion from the high-frequency APE, but their consumption is mostly through eddy advection of geopotential anomalies with relatively small transformation into low-frequency KE. The budget term of low-frequency KE shows no clear signals contributing to its long-term changes, which may partially explain the opposite trends of jet stream changes in previous studies (Wang et al. 2017; Franzke and Harnik 2023).

In summary, this work provides a first systematic attempt to depict the climatology and long-term changes in a local energetic framework developed by Novak and Tailleux (2018). The physical understanding of this local framework is consistent with the classic Lorenz energy cycle and more importantly provides insights about the interactions between APE and KE on different spatiotemporal scales. Moreover, the budget for various energetic forms is balanced quite well, both globally and locally. We acknowledge that only one dataset (i.e., ERA5) is used in this study. The robustness of the findings needs to be verified using other reanalysis products. Further applications of this framework in the context of teleconnection patterns (Kosaka et al. 2009), storm tracks (Mbengue and Schneider 2017), extratropical cyclone activities (Gertler and O'Gorman 2019), and monsoons (Hu et al. 2022) will be studied in the future. It is also interesting to evaluate the model performance on this local energetics and project their future changes under different socioeconomic scenarios. A moist version which explicitly considers the moisture effect can also be explored by using equivalent potential temperature or virtual temperature (Lembo et al. 2019; Harris et al. 2022). While using only virtual temperature to account for moist processes is potentially a limitation, this framework might still produce an effectively closed budget enabling physical insights into moist energetics.

Acknowledgments. The authors thank Editor Jian Lu and two anonymous reviewers whose constructive comments led to a significant improvement of the manuscript. We thank Dr. Nili Harnik for helpful discussions. This study was supported by the Institute for Basic Science (IBS), South Korea, under IBS-R028-D1. ZL is supported by the start-up funding of the Hong Kong University of Science and Technology (Guangzhou), the National Natural Science Foundation of China (42405020), and the Guangzhou Municipal Science and Technology Project for Maiden Voyage (2024A04J4523). CF is supported by the National Research Fund of Korea

(NRF-2022M3K3A109708). LN is supported by Schmidt Sciences. VL acknowledges financial support by project DROMEDAR-Grant Assignment Decree No. 1388 by the Italian Ministry of University and Research (MUR) under the National Recovery and Resilience Plan (NRRP), Mission 4, Component 2, Investment 1.1, Call for tender n. 1409, funded by the European Union-NextGenerationEU, and funding from the Italian Ministry of Education, University and Research (MIUR) through the JPI Oceans and JPI Climate "Next Generation Climate Science in Europe for Oceans"-ROADMAP project (D. M. 593/2016) and from the European Union's Horizon Europe research and innovation program Grant 101081193 (OptimESM). The analysis was conducted on the IBS/ICCP supercomputer "Aleph," 1.43 petaflop high-performance Cray XC50-LC Skylake computing system with 18,720 processor cores, 9.59 PB storage, and 43 PB tape archive space. We also acknowledge the support of KREONET.

Data availability statement. The ERA5 reanalysis product is available online from the website https://www.ecmwf.int/en/forecasts/dataset/ecmwf-reanalysis-v5.

REFERENCES

Ahbe, E., and K. Caldeira, 2017: Spatial distribution of generation of Lorenz's available potential energy in a global climate model. *J. Climate*, **30**, 2089–2101, https://doi.org/10.1175/JCLI-D-15-0614.1.

Andrews, D. G., 1981: A note on potential energy density in a stratified compressible fluid. *J. Fluid Mech.*, **107**, 227–236, https://doi.org/10.1017/S0022112081001754.

Boer, G. J., and S. Lambert, 2008: The energy cycle in atmospheric models. *Climate Dyn.*, **30**, 371–390, https://doi.org/10.1007/s00382-007-0303-4.

Bordbar, M. H., T. Martin, M. Latif, and W. Park, 2017: Role of internal variability in recent decadal to multidecadal tropical Pacific climate changes. *Geophys. Res. Lett.*, **44**, 4246–4255, https://doi.org/10.1002/2016GL072355.

Broström, G., K. H. Christensen, M. Drivdal, and J. E. H. Weber, 2014: Note on Coriolis-Stokes force and energy. *Ocean Dyn.*, **64**, 1039–1045, https://doi.org/10.1007/s10236-014-0723-8.

Chang, E. K. M., C.-G. Ma, C. Zheng, and A. M. W. Yau, 2016: Observed and projected decrease in Northern Hemisphere extratropical cyclone activity in summer and its impacts on maximum temperature. *Geophys. Res. Lett.*, **43**, 2200–2208, https://doi.org/10.1002/2016GL068172.

Chemke, R., and L. M. Polvani, 2020: Linking midlatitudes eddy heat flux trends and polar amplification. *npj Climate Atmos. Sci.*, **3**, 8, https://doi.org/10.1038/s41612-020-0111-7.

Chung, E.-S., A. Timmermann, B. J. Soden, K.-J. Ha, L. Shi, and V. O. John, 2019: Reconciling opposing Walker circulation trends in observations and model projections. *Nat. Climate Change*, **9**, 405–412, https://doi.org/10.1038/s41558-019-0446-4.

Colle, B. A., F. Buonaiuto, M. J. Bowman, R. E. Wilson, R. Flood, R. Hunter, A. Mintz, and D. Hill, 2008: New York City's vulnerability to coastal flooding: Storm surge modeling of past cyclones. *Bull. Amer. Meteor. Soc.*, **89**, 829–842, https://doi.org/10.1175/2007BAMS2401.1.

Coumou, D., G. Di Capua, S. Vavrus, L. Wang, and S. Wang, 2018: The influence of Arctic amplification on mid-latitude summer circulation. *Nat. Commun.*, **9**, 2959, https://doi.org/10.1038/s41467-018-05256-8.

Dannenberg, M. P., and E. K. Wise, 2017: Shifting Pacific storm tracks as stressors to ecosystems of western North America. *Global Change Biol.*, **23**, 4896–4906, https://doi.org/10.1111/gcb.13748.

Duchon, C. E., 1979: Lanczos filtering in one and two dimensions. *J. Appl. Meteor.*, **18**, 1016–1022, https://doi.org/10.1175/1520-0450(1979)018<1016:LFIOAT>2.0.CO;2.

England, M. H., and Coauthors, 2014: Recent intensification of wind-driven circulation in the Pacific and the ongoing warming hiatus. *Nat. Climate Change*, **4**, 222–227, https://doi.org/10.1038/nclimate2106.

Fan, W., Y. Liu, A. Chappell, L. Dong, R. Xu, M. Ekström, T.-M. Fu, and Z. Zeng, 2021: Evaluation of global reanalysis land surface wind speed trends to support wind energy development using in situ observations. *J. Appl. Meteor. Climatol.*, **60**, 33–50, https://doi.org/10.1175/JAMC-D-20-0037.1.

Faranda, D., V. Lembo, M. Iyer, D. Kuzzay, S. Chibbaro, F. Daviaud, and B. Dubrulle, 2018: Computation and characterization of local subfilter-scale energy transfers in atmospheric flows. *J. Atmos. Sci.*, **75**, 2175–2186, https://doi.org/10.1175/JAS-D-17-0114.1.

Feldstein, S. B., 2002: Fundamental mechanisms of the growth and decay of the PNA teleconnection pattern. *Quart. J. Roy. Meteor. Soc.*, **128**, 775–796, https://doi.org/10.1256/003590002164368 3.

——, 2003: The dynamics of NAO teleconnection pattern growth and decay. *Quart. J. Roy. Meteor. Soc.*, **129**, 901–924, https://doi.org/10.1256/qj.02.76.

Franzke, C. L. E., and N. Harnik, 2023: Long-term trends of the atmospheric circulation and moist static energy budget in the JRA-55 reanalysis. *J. Climate*, **36**, 2959–2984, https://doi.org/10.1175/JCLI-D-21-0724.1.

——, and Coauthors, 2020: The structure of climate variability across scales. *Rev. Geophys.*, **58**, e2019RG000657, https://doi.org/10.1029/2019RG000657.

Gertler, C. G., and P. A. O'Gorman, 2019: Changing available energy for extratropical cyclones and associated convection in Northern Hemisphere summer. *Proc. Natl. Acad. Sci. USA*, **116**, 4105–4110, https://doi.org/10.1073/pnas.1812312116.

Gualtieri, G., 2022: Analysing the uncertainties of reanalysis data used for wind resource assessment: A critical review. *Renewable Sustainable Energy Rev.*, **167**, 112741, https://doi.org/10.1016/j.rser.2022.112741.

Harris, B. L., R. Tailleux, C. E. Holloway, and P. L. Vidale, 2022: A moist available potential energy budget for an axisymmetric tropical cyclone. *J. Atmos. Sci.*, **79**, 2493–2513, https://doi.org/10.1175/JAS-D-22-0040.1.

Hersbach, H., and Coauthors, 2020: The ERA5 global reanalysis. *Quart. J. Roy. Meteor. Soc.*, **146**, 1999–2049, https://doi.org/10.1002/qj.3803.

Holliday, D., and M. E. McIntyre, 1981: On potential energy density in an incompressible, stratified fluid. *J. Fluid Mech.*, **107**, 221–225, https://doi.org/10.1017/S0022112081001742.

Holopainen, E. O., 1978: A diagnostic study on the kinetic energy balance of the long-term mean flow and the associated transient fluctuations in the atmosphere. *Geophysica*, **15**, 125–145.

Hu, P., W. Chen, Z. Li, S. Chen, L. Wang, and Y. Liu, 2022: Close linkage of the South China Sea summer monsoon onset and extreme rainfall in may over Southeast Asia: Role of the synoptic-scale systems. *J. Climate*, **35**, 4347–4362, https://doi.org/10.1175/JCLI-D-21-0740.1.

Kållberg, P., P. Berrisford, B. Hoskins, A. Simmons, S. Uppala, S. Lamy-thépaut, and R. Hine, 2005: ERA-40 Atlas. ERA-40 Project Rep. Series 19, ECMWF, 199 pp.

Kanno, Y., and T. Iwasaki, 2022: Future changes of atmospheric energy cycle in CMIP5 climate models. *J. Geophys. Res. Atmos.*, **127**, e2021JD036380, https://doi.org/10.1029/2021JD036380.

——, M. R. Abdillah, and T. Iwasaki, 2016: Long-term trend of cold air mass amount below a designated potential temperature in Northern and Southern Hemispheric winters using reanalysis data sets. *J. Geophys. Res. Atmos.*, **121**, 10 138–10 152, https://doi.org/10.1002/2015JD024635.

Kim, Y.-H., and M.-K. Kim, 2013: Examination of the global Lorenz energy cycle using MERRA and NCEP-reanalysis 2. *Climate Dyn.*, **40**, 1499–1513, https://doi.org/10.1007/s00382-012-1358-4.

Kosaka, Y., H. Nakamura, M. Watanabe, and M. Kimoto, 2009: Analysis on the dynamics of a wave-like teleconnection pattern along the summertime Asian jet based on a reanalysis dataset and climate model simulations. *J. Meteor. Soc. Japan*, **87**, 561–580, https://doi.org/10.2151/jmsj.87.561.

Kretschmer, M., D. Coumou, L. Agel, M. Barlow, E. Tziperman, and J. Cohen, 2018: More-persistent weak stratospheric polar vortex states linked to cold extremes. *Bull. Amer. Meteor. Soc.*, **99**, 49–60, https://doi.org/10.1175/BAMS-D-16-0259.1.

Kucharski, F., and A. J. Thorpe, 2000: Local energetics of an idealized baroclinic wave using extended exergy. *J. Atmos. Sci.*, **57**, 3272–3284, https://doi.org/10.1175/1520-0469(2000)057<3272:LEOAIB>2.0.CO;2.

Lau, N.-C., and A. H. Oort, 1982: A comparative study of observed Northern Hemisphere circulation statistics based on GFDL and NMC analyses. Part II: Transient eddy statistics and the energy cycle. *Mon. Wea. Rev.*, **110**, 889–906, https://doi.org/10.1175/1520-0493(1982)110<0889:ACSOON>2.0.CO;2.

Lembo, V., F. Lunkeit, and V. Lucarini, 2019: TheDiaTo (v1.0)—A new diagnostic tool for water, energy and entropy budgets in climate models. *Geosci. Model Dev.*, **12**, 3805–3834, https://doi.org/10.5194/gmd-12-3805-2019.

Li, L., A. P. Ingersoll, X. Jiang, D. Feldman, and Y. L. Yung, 2007: Lorenz energy cycle of the global atmosphere based on reanalysis datasets. *Geophys. Res. Lett.*, **34**, L16813, https://doi.org/10.1029/2007GL029985.

Lorenz, E. N., 1955a: Generation of available potential energy and the intensity of the general circulation. University of California, Los Angeles, Dept. of Meteorology Tech. Rep. AF19, 36 pp.

——, 1955b: Available potential energy and the maintenance of the general circulation. *Tellus*, **7A**, 157–167, https://doi.org/10.3402/tellusa.v7i2.8796.

Lovejoy, S., 2019: *Weather, Macroweather, and the Climate: Our Random yet Predictable Atmosphere*. Oxford University Press, 334 pp.

Lucarini, V., K. Fraedrich, and F. Lunkeit, 2010: Thermodynamics of climate change: Generalized sensitivities. *Atmos. Chem. Phys.*, **10**, 9729–9737, https://doi.org/10.5194/acp-10-9729-2010.

Ma, Q., V. Lembo, and C. L. E. Franzke, 2021: The Lorenz energy cycle: Trends and the impact of modes of climate variability. *Tellus*, **73A**, 1900033, https://doi.org/10.1080/16000870.2021.1900033.

Marques, C. A. F., A. Rocha, and J. Corte-Real, 2010: Comparative energetics of ERA-40, JRA-25 and NCEP-R2 reanalysis, in the wave number domain. *Dyn. Atmos. Oceans*, **50**, 375–399, https://doi.org/10.1016/j.dynatmoce.2010.03.003.

Mbengue, C., and T. Schneider, 2017: Storm-track shifts under climate change: Toward a mechanistic understanding using baroclinic mean available potential energy. *J. Atmos. Sci.*, **74**, 93–110, https://doi.org/10.1175/JAS-D-15-0267.1.

McGregor, S., A. Timmermann, M. F. Stuecker, M. H. England, M. Merrifield, F.-F. Jin, and Y. Chikamoto, 2014: Recent Walker circulation strengthening and Pacific cooling amplified by Atlantic warming. *Nat. Climate Change*, **4**, 888–892, https://doi.org/10.1038/nclimate2330.

Michaelides, S., 2021: Lorenz atmospheric energy cycle in climatic projections. *Climate*, **9**, 180, https://doi.org/10.3390/cli9120180.

Novak, L., 2016: The lifecycle of storm tracks. Ph.D. thesis, University of Reading, 127 pp.

——, and R. Tailleux, 2018: On the local view of atmospheric available potential energy. *J. Atmos. Sci.*, **75**, 1891–1907, https://doi.org/10.1175/JAS-D-17-0330.1.

Oort, A. H., 1964: On estimates of the atmospheric energy cycle. *Mon. Wea. Rev.*, **92**, 483–493, https://doi.org/10.1175/1520-0493(1964)092<0483:OEOTAE>2.3.CO;2.

——, and J. P. Peixoto, 1976: On the variability of the atmospheric energy cycle within a 5-year period. *J. Geophys. Res.*, **81**, 3643–3659, https://doi.org/10.1029/JC081i021p03643.

Orlanski, I., and J. Katzfey, 1991: The life cycle of a cyclone wave in the Southern Hemisphere. Part I: Eddy energy budget. *J. Atmos. Sci.*, **48**, 1972–1998, https://doi.org/10.1175/1520-0469(1991)048<1972:TLCOAC>2.0.CO;2.

Oudar, T., J. Cattiaux, and H. Douville, 2020: Drivers of the northern extratropical eddy-driven jet change in CMIP5 and CMIP6 models. *Geophys. Res. Lett.*, **47**, e2019GL086695, https://doi.org/10.1029/2019GL086695.

Pan, Y., L. Li, X. Jiang, G. Li, W. Zhang, X. Wang, and A. P. Ingersoll, 2017: Earth's changing global atmospheric energy cycle in response to climate change. *Nat. Commun.*, **8**, 14367, https://doi.org/10.1038/ncomms14367.

Peixóto, J. P., and A. H. Oort, 1974: The annual distribution of atmospheric energy on a planetary scale. *J. Geophys. Res.*, **79**, 2149–2159, https://doi.org/10.1029/JC079i015p02149.

Persson, A. O., 2005: The Coriolis effect: Four centuries of conflict between common sense and mathematics. *Hist. Meteor.*, **2**, 1–24.

Priestley, M. D. K., and J. L. Catto, 2022: Future changes in the extratropical storm tracks and cyclone intensity, wind speed, and structure. *Wea. Climate Dyn.*, **3**, 337–360, https://doi.org/10.5194/wcd-3-337-2022.

Schneider, T., T. Bischoff, and G. H. Haug, 2014: Migrations and dynamics of the intertropical convergence zone. *Nature*, **513**, 45–53, https://doi.org/10.1038/nature13636.

Serreze, M. C., A. P. Barrett, J. C. Stroeve, D. N. Kindig, and M. M. Holland, 2009: The emergence of surface-based Arctic amplification. *Cryosphere*, **3**, 11–19, https://doi.org/10.5194/tc-3-11-2009.

Shepherd, T. G., 1993: A unified theory of available potential energy. *Atmos.–Ocean*, **31**, 1–26, https://doi.org/10.1080/07055900.1993.9649460.

——, 2016: Effects of a warming Arctic. *Science*, **353**, 989–990, https://doi.org/10.1126/science.aag2349.

Simmons, A. J., 2022: Trends in the tropospheric general circulation from 1979 to 2022. *Wea. Climate Dyn.*, **3**, 777–809, https://doi.org/10.5194/wcd-3-777-2022.

Simpson, I. R., R. Seager, M. Ting, and T. A. Shaw, 2016: Causes of change in Northern Hemisphere winter meridional winds

and regional hydroclimate. *Nat. Climate Change*, **6**, 65–70, https://doi.org/10.1038/nclimate2783.

Sohn, B. J., and S.-C. Park, 2010: Strengthened tropical circulations in past three decades inferred from water vapor transport. *J. Geophys. Res.*, **115**, D15112, https://doi.org/10.1029/2009JD013713.

Tailleux, R., 2013: Available potential energy and exergy in stratified fluids. *Annu. Rev. Fluid Mech.*, **45**, 35–58, https://doi.org/10.1146/annurev-fluid-011212-140620.

——, 2018: Local available energetics of multicomponent compressible stratified fluids. *J. Fluid Mech.*, **842**, R1, https://doi.org/10.1017/jfm.2018.196.

Takahashi, C., and M. Watanabe, 2016: Pacific trade winds accelerated by aerosol forcing over the past two decades. *Nat. Climate Change*, **6**, 768–772, https://doi.org/10.1038/nclimate2996.

Trenberth, K. E., J. T. Fasullo, and J. Kiehl, 2009: Earth's global energy budget. *Bull. Amer. Meteor. Soc.*, **90**, 311–324, https://doi.org/10.1175/2008BAMS2634.1.

Wang, J., H.-M. Kim, and E. K. M. Chang, 2017: Changes in Northern Hemisphere winter storm tracks under the background of Arctic amplification. *J. Climate*, **30**, 3705–3724, https://doi.org/10.1175/JCLI-D-16-0650.1.